

Article

Pitch/Metal Oxide Composite Fibers via Electrospinning for Environmental Applications

Bayan Kaidar^{1,2}, Gaukhar Smagulova^{1,2,*} , Aigerim Imash^{1,2} , Aruzhan Keneshbekova¹, Akram Ilyanov² and Zulkhair Mansurov^{1,2}

¹ Laboratory of Functional Nanomaterials, Institute of Combustion Problems, Almaty 050012, Kazakhstan; kaidar.bayan@gmail.com (B.K.); iimash.aigerim@gmail.com (A.I.); keneshbekova.a0204@gmail.com (A.K.); zmansurov@kaznu.kz (Z.M.)

² Department of Chemical Physics and Material Science, Faculty of Chemistry and Chemical Technology, Al-Farabi Kazakh National University, Almaty 050040, Kazakhstan; akram.ily04@gmail.com

* Correspondence: smagulova.gaukhar@gmail.com; Tel.: +7-707-566-6345

Abstract: This study investigates the synthesis and application of composite electrospun fibers incorporating coal tar pitch (CTP) and various nanomaterial additives, with a specific focus on their potential for eco-bio-applications. The research underscores the environmentally viable aspects of CTP following a thermal treatment process that eliminates volatile components and sulfur, rendering it amenable for fiber electrospinning and subsequent carbonization. Composite fibers were fabricated by integrating CTP with nanomaterials, including nickel oxide (NiO), titanium dioxide (TiO₂), activated carbon (AC), and magnetite (Fe₃O₄). The C/NiO composite fibers exhibit notable acetone sensing capabilities, specifically displaying a rapid response time of 40.6 s to 100 ppm acetone at 220 °C. The C/TiO₂ composite fibers exhibit a distinct “beads-on-a-string” structure and demonstrate a high efficiency of 96.13% in methylene blue decomposition, highlighting their potential for environmental remediation applications. Additionally, the C/AC composite fibers demonstrate effective adsorption properties, efficiently removing manganese (II) ions from aqueous solutions with an 88.62% efficiency, thereby suggesting their utility in water purification applications. This research employs an interdisciplinary approach by combining diverse methods, approaches, and materials, including the utilization of agricultural waste materials such as rice husks, to create composite materials with multifaceted applications. Beyond the immediate utility of the composite fibers, this study emphasizes the significance of deploying environmentally responsible materials and technologies to address pressing eco-bio-challenges.

Keywords: electrospinning; coal tar pitch; nickel oxide; magnetite; activated carbon; titanium oxide; gas sensor; photocatalyst; adsorption



Citation: Kaidar, B.; Smagulova, G.; Imash, A.; Keneshbekova, A.; Ilyanov, A.; Mansurov, Z. Pitch/Metal Oxide Composite Fibers via Electrospinning for Environmental Applications. *Technologies* **2023**, *11*, 156. <https://doi.org/10.3390/technologies11060156>

Academic Editors: Manoj Gupta and Yury A. Skorik

Received: 2 October 2023

Revised: 25 October 2023

Accepted: 30 October 2023

Published: 7 November 2023



Copyright: © 2023 by the authors. Licensee MDPI, Basel, Switzerland. This article is an open access article distributed under the terms and conditions of the Creative Commons Attribution (CC BY) license (<https://creativecommons.org/licenses/by/4.0/>).

1. Introduction

The global pursuit of environmental sustainability has led to transformative innovation. In this era, eco-bio-applications, driven by novel materials and advanced technologies, play a pivotal role in our collective effort to achieve a sustainable future. With climate change, pollution, resource depletion, and biodiversity loss as pressing issues, the demand for innovative, environmentally conscious approaches is urgent [1]. Eco-bio-applications represent a paradigm shift by seamlessly integrating ecological and biological principles with cutting-edge materials and techniques. In this context, the synthesis and use of new materials will be vital in bridging the gap between human progress and planetary preservation.

Sustainable development, as championed with the United Nations' Sustainable Development Goals (SDGs), demands a holistic consideration of the environmental, social, and economic dimensions [2]. New technologies and materials, especially in the composite nanomaterials field, offer great potential in tackling these challenges. Composite nanomaterials within nanotechnology offer diverse shapes and combinations, elevating

synthesis methodologies to new levels. This burgeoning field hinges on three key aspects: the composition and structure, fabrication methods, and various application domains of nanocomposites. Combining options within these dimensions provides a wide spectrum of tailored composite forms for diverse applications.

This paper centers on the production of composites via the electrospinning technique for eco-bio-applications. Bioecology, as a subfield of ecology, delves into the interplay between the environment and biological organisms.

Electrospinning stands out as a versatile technique capable of producing one-dimensional (1D) monocomponent and composite fibers, spanning an extensive spectrum of materials, from biopolymers [3] to metals and alloys [4]. These electrospun fibers have found applications across diverse fields, reflecting the adaptability and utility of this method. For a comprehensive exploration of electrospun fiber applications, extensive reviews are available [5–9]. In this context, a concise overview of research on the current use of electrospun fibers in eco-bio-applications is presented below, taking a closer look at electrospun fibers with the addition of nickel oxide, titanium oxide, activated carbon, and magnetite for environmental applications.

The composite nanofibers enhance the water purification process by effectively filtering and retaining fouling particles. A variety of nanofiber composite membranes, including carbon [10], nylon [11], polysulfone [12], cellulose [13], as well as polymers such as polyacrylonitrile (PAN) [14], polyvinylidene fluoride (PVDF) [15], polytetrafluoroethylene (PTFE) [16], and polypropylene (PP) [17] exhibit high performance in removing contaminants from water. Modifying these membranes enhances their performance and reduces fouling. Nanofibers show significant potential in the effective purification of water, positioning them as essential materials for future water treatment technologies.

Electrospun nanofiber membranes have the capacity to remove heavy metals, large particles, bacteria, viruses, and other textile debris, making them well-suited for water purification. Functionalizing these membranes with nanoparticles and additives such as activated carbon can address fouling issues by enhancing the effectiveness of nanostructures. This is due to several unique properties, including a lower volume-to-surface area ratio, where in the nanoscale, the number of atoms on the surface increases while defects decrease [18–20].

The application of nanofiber/activated carbon (AC) composites in water treatment processes is recognized as one of the most effective methods for removing various contaminants from aqueous solutions. Within these composites, activated carbon serves a crucial role by absorbing and retaining various contaminants due to its high active surface area and porous structure. In a study conducted by Shahrokhi-Shahraki et al. [21], activated carbon derived from tires was employed to purify water contaminated with synthetic heavy metals, including Pb^{2+} , Cu^{2+} , and Zn^{2+} . The data obtained confirm that this activated carbon demonstrates significant potential for adsorbing heavy metals, with adsorption capacities of 322.5 mg/g for Pb^{2+} , 185.2 mg/g for Cu^{2+} , and 71.9 mg/g for Zn^{2+} , respectively. It has also been observed that other factors such as the presence of other ions, amorphousness, crystallinity of the material, and pore size influence the adsorption capacity of sorbents. In the case of mesopores, the adsorption mechanism begins with the formation of a monolayer on the activated carbon surface, followed by pore condensation. Heavy metals are retained through ion exchange and chemical adsorption mechanisms [22]. To enhance the efficiency of water purification, an important factor is the high content of functional groups or active centers on the activated carbon surface, capable of binding heavy metals. Furthermore, the presence of cations like K^+ , Ca^{2+} , and Mg^{2+} in activated carbon, which can exchange with toxic metal ions, further promotes heavy metal adsorption through ion exchange mechanisms [21].

In addition to adsorption methods for purifying water from contaminants, photocatalytic decomposition is regarded as a promising technique. Among the myriad of purification technologies, photocatalysis has proven to be a powerful approach and titanium dioxide (TiO_2) stands out as a leading photocatalyst due to its non-toxicity, excep-

tional photoactivity, and low cost [23]. However, despite TiO₂'s remarkable photocatalytic capabilities, its full potential is often hindered by several limitations, such as the rapid recombination of photogenerated electron–hole pairs and the restricted light absorption in the ultraviolet (UV) range [24]. To overcome these hurdles and enhance TiO₂'s photocatalytic performance, the incorporation of carbon nanofibers has emerged as a transformative solution. TiO₂/carbon nanofiber composites have garnered substantial attention in recent years for their ability to synergize the merits of TiO₂ and carbon-based materials, effectively addressing the shortcomings of traditional TiO₂ photocatalysts. Due to this, most of the researchers have implemented electrospinning technology [25–27], which has demonstrated outstanding outcomes in the treatment of wastewater containing different kinds of dyes.

In reference [28], an excellent example of using a combination of TiO₂ and metal–organic frameworks, specifically zeolitic imidazolate framework-8 (ZIF-8), is presented. This combination was prepared using ultrasonic and electrospinning methods, demonstrating good photoactivity and the ability to maintain its performance over multiple cycles (88.7% efficiency after five cycles). The use of multilayer composites, including TiO₂, carbon nanotubes, and polymethyl methacrylate, created using the same electrospinning method, can enhance the photocatalysis effect for a broader range of dyes, expanding its application scope [29]. Furthermore, a novel photocatalyst [30], known as Janus nanofiber heterojunction photocatalysts (JNHPs), was developed. JNHP incorporates a TiO₂/C nanofiber side that responds to UV light and a Bi₂WO₆/C nanofiber side that is responsive to visible light, efficiently utilizing sunlight. JNHP excels in hydrogen production and methylene blue degradation without the need for noble metals as co-catalysts. This approach holds promise for the development of other bifunctional nanofiber photocatalysts.

Composite nanomaterials find critical applications in the detection of hazardous gases, including toxic, flammable, and explosive substances [31–34]. Recent interest has centered on gas sensors utilizing carbon fibers and metal oxide nanoparticles, particularly NiO, renowned for their simple production methods and high selectivity [35].

NiO-based gas sensors operate by measuring resistance changes in the sensing layer upon gas molecule adsorption. Nanofibers, with their exceptional surface-to-volume ratio, high porosity, and enhanced active centers, improve gas adsorption, enhancing gas detection performance [36]. Among various nanofiber fabrication methods, electrospinning stands out as a promising, cost-effective, and versatile technique for producing NiO-based composite nanofibers. These nanofibers enhance electrical transport, specific surface area, and contact area with the target gas, and reduce charge transfer time, making them highly suitable for gas sensor development.

In [37], PAN/NiO-based gas sensors were successfully used for methanol detection, demonstrating high selectivity and stability. Gas sensors not only find application in environmental protection but also in biomedicine. For instance, poly(vinyl alcohol) (PVA)/NiO nanofibers produced using electrospinning exhibited a rapid response and recovery time, making them suitable for formaldehyde vapor detection [38]. Electrospun NiO nanograins can be utilized in exhaled air sensors for lung disease diagnoses [39]. Incorporating electrospun nanomaterials into gas sensors results in ultrahigh sensitivity, excellent selectivity, long-term stability, and cost-effectiveness even in challenging conditions.

The potential utilization of magnetic composite fibers, particularly those incorporating magnetite nanoparticles, is determined with their physicochemical and magnetic characteristics. These properties make them remarkably versatile and applicable in a wide range of fields, including sensing, biomedicine, electronics, telecommunications, environmental protection, and energy storage, as discussed in references [40,41]. For example, composite fibers containing magnetite nanoparticles exhibit a significant level of magnetization, a crucial characteristic that underscores their usefulness [42]. It is worth noting that the inclusion of magnetite nanoparticles not only enhances the dielectric properties and magnetic characteristics of the fibers but also exerts influence over their orientation and size. This study also investigated the effects of magnetic fields on fiber orientation during the electrospinning process, resulting in reduced fiber dimensions and improved fiber alignment [43].

In references [44,45], composite fibers based on magnetite nanoparticles in poly(ethylene oxide) (PEO) and polydopamine (PDA) matrices were fabricated through electrospinning for the removal of Pb(II) ions from solutions. Reference [46] discusses the production of polyvinylpyrrolidone (PVP)/Fe₃O₄ fibers for drug delivery as drug-loaded magnetic materials. Additionally, PVA/Fe₃O₄ fibers, as described in [47], can be used for physisorption, and they also serve as biomembranes, as discussed in [48]. Alginate/Fe₃O₄ electrospun fibers, as demonstrated in reference [49], find applications in adsorption and separation of antibiotics, including the separation of ciprofloxacin hydrochloride from aqueous solutions. As a result, the growing body of research dedicated to the development of functional magnetic fibers, distinguished by their exceptional magnetic properties attributed to the presence of magnetite nanoparticles, is indeed significant.

This article presents the results obtained by the Institute of Combustion Problems research group regarding the synthesis of composite materials using the electrospinning method and their environmental applications. The study involved the preparation of carbon-based composite fibers with the addition of MOx (NiO, TiO₂, and Fe₃O₄), as well as carbon-carbon fibers through the incorporation of activated carbon particles. The resulting fibers were subject to testing for the purification of water from metal ions and organic pollutants through adsorption and photocatalytic decomposition. Additionally, the fibers were evaluated for their capability to detect toxic gases in the atmosphere. One noteworthy aspect of this study is the use of coal tar pitch in conjunction with the primary PAN solution as an alternative, cost-effective precursor. Furthermore, the production of activated carbon is involved in the use of agricultural waste, specifically rice husk. This illustrates the potential for converting industrial and agricultural waste materials into environmentally protective materials.

2. Materials and Methods

This investigation involves multiple experimental phases, which can be categorized into three primary stages:

1. Synthesis of basic components intended for subsequent composite material fabrication.
2. Synthesis of composite fibers through electrospinning and their subsequent heat treatment.
3. Evaluation and practical implementation of the resulting materials.

It is important to note that each stage incorporates fundamental techniques for examining intermediate and final products, including morphological and physicochemical analyses. Some of these steps are illustrated in Figure 1.

2.1. Production of Coal Tar Pitches (CTPs) with Thermal Treatment

Coal tar pitches were obtained through the thermal conversion of coal tar in a tube furnace equipped with a quartz reactor under an inert atmosphere. To investigate the influence of temperature on pitch formation, heat treatment was carried out within the temperature range of 200–500 °C, while maintaining an argon gas flow rate of 90–92 cm³/min. A pre-dried and accurately weighed porcelain or quartz boat was loaded with coal tar, and its initial mass was recorded for a subsequent mass loss analysis. The boat containing the coal tar was then placed into the reactor and subjected to argon purging to eliminate atmospheric air. Argon purging was maintained for 5 min, after which the reactor was gradually heated to the specified temperature range (200–500 °C). The temperature treatment duration was set at 1 h. Once the heat treatment was completed, the reactor heating was turned off, and the sample was allowed to cool to ambient temperature within an argon-filled environment. After extraction, the product boat was re-weighed to measure the mass loss. Subsequently, the resulting material was used for electrospinning to produce fibers.

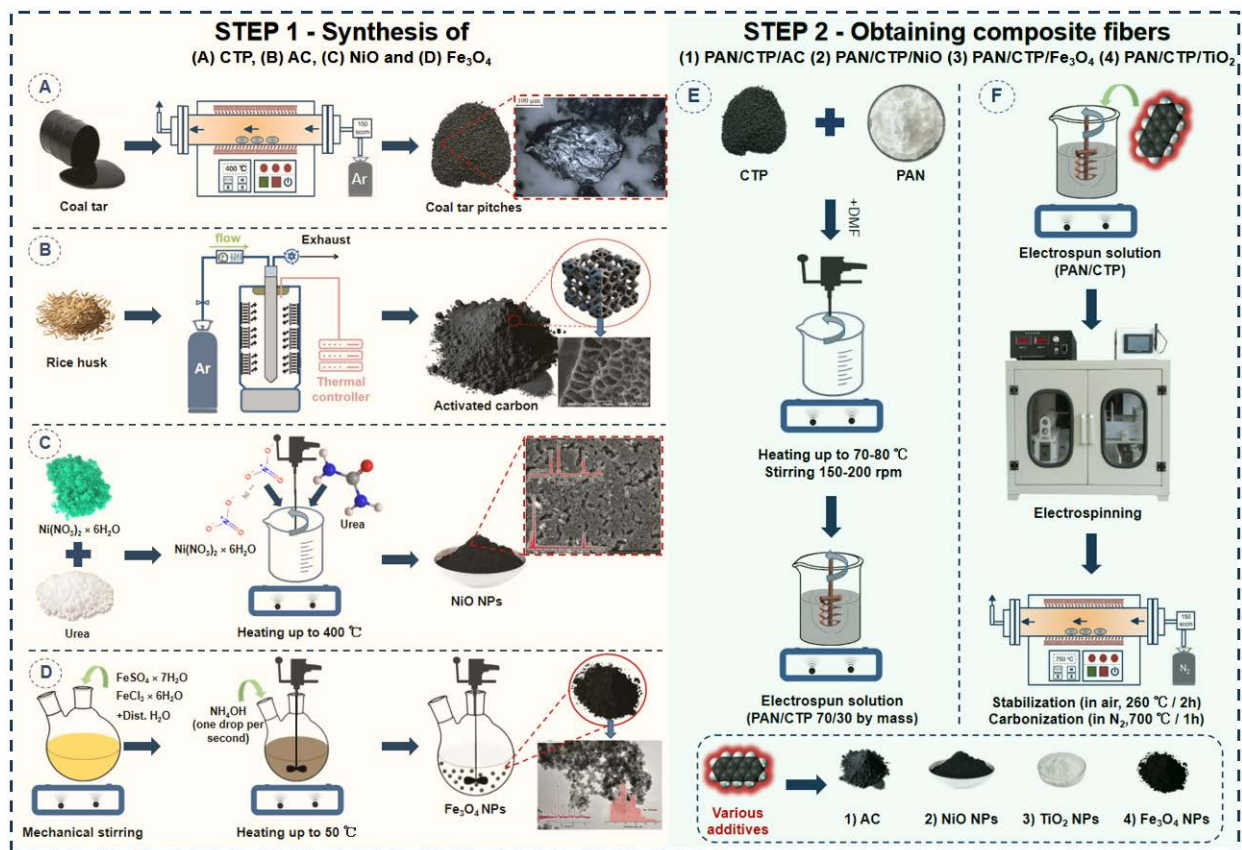


Figure 1. The key stages involved in the production of various composite fibers. (A)—Synthesis of coal tar pitches from coal tar by heat treatment; (B)—Synthesis of activated carbon from rice husk; (C)—Solution-combustion synthesis of nickel oxide nanoparticles; (D)—Synthesis of magnetite nanoparticles by chemical condensation; (E)—Preparation of electroforming solution based on PAN and CTP; (F)—Preparation of PAN/CTP-based carbon fibres incorporating diverse additives such as activated carbon, NiO, TiO₂ and Fe₃O₄.

2.2. Synthesis of C/NiO Composite Fibers

Nickel oxide nanoparticles were synthesized using the solution combustion method. Nickel nitrate hexahydrate (Ni(NO₃)₂·6H₂O) was employed as the oxidizer, and urea (NH₂CONH₂) as the fuel. The process commenced by dissolving these reagents in distilled water and evaporating the solution to a final volume of 5–7 mL, resulting in a gel-like substance as most of the water evaporated. Subsequently, the mixture was heated to 260 °C, causing spontaneous ignition. The choice of ignition temperature was based on urea's decomposition point, which can reach temperatures of up to 1200 °C in the burning zone. This led to the deposition of the final product on the inner surfaces of the glassware, yielding a fine, jet-black powder.

To prepare a fiber-forming PAN and CTP solution with nickel oxide nanoparticles, the following steps were followed:

1. A well-suited suspension of powdered PAN was combined with N,N-dimethylformamide (DMF) in a mass ratio of 9:1. This mixture was stirred on a magnetic stirrer at 150 rpm and maintained within a temperature range of 70–80 °C for 2 h until a homogeneous solution was achieved.
2. Once complete homogenization was achieved, the PAN solution was blended with small quantities of CTP in a mass ratio of 70:30. The resulting mixture underwent ultrasonic treatment in a bath operating at a temperature range of 70–80 °C for 60 min, ensuring the uniform dispersion of CTP within the polymer solution.

3. Subsequently, nickel oxide powder was added to the solution, maintaining a weight ratio of 70:30 ((PAN/CTP):NiO). This suspension was continuously stirred on a magnetic stirrer for a duration of 12 h.

The electrospinning process was conducted using a specialized apparatus consisting of a solution delivery system, a syringe reservoir equipped with a metal needle, a power source, and a variable-speed drum collector. The fiber formation procedure was carried out under ambient conditions, with a temperature range of 20–30 °C and a relative humidity of 30–40%.

The polymer solution was loaded into a 5 mL syringe, with a metal needle securely attached to its end. A negative voltage was applied to the needle, while a positive voltage was applied to the collector. Specifically, both the needle and the drum collector were subjected to a voltage of 15 kV. The solution feed rate was maintained at 1.0 mL/h, the drum collector had a radius of 20 cm, and the distance between the needle and the collector was set at 15 cm. To facilitate fiber deposition, the collector's surface was lined with aluminum foil. Voltage levels and the distance between the electrode and the collector were meticulously adjusted to ensure the stable formation of the electrospinning jet. Subsequently, the fibers underwent a two-step process involving stabilization and carbonization.

For stabilization, the PAN/CTP/NiO fibers were placed in a tubular CVD (Chemical Vapor Deposition) furnace with a quartz tube, heated to 260 °C, and kept at this temperature for 1 h in an air atmosphere. Afterward, the furnace was turned off, and the sample was allowed to cool to room temperature inside the furnace.

Subsequently, carbonization was carried out in the same CVD furnace. The quartz tube was purged with high-purity nitrogen (99.993%) to eliminate any traces of air and prevent contact with oxygen. The furnace was then heated to 700 °C, and the carbonization process lasted for 1 h. After completion, the furnace was turned off, and the sample was cooled to room temperature in a nitrogen atmosphere, again without removal from the reactor. The obtained sample was named "C/NiO fibers".

To assess the gas sensitivity, the C/NiO fibers were meticulously ground in an agate mortar. The ground composite fibers were blended with PVDF at a mass ratio of 85:15 (C/NiO:PVDF), with PVDF serving as a binding agent in the mixture. The resulting viscous suspension was applied onto a microchip specially designed with interdigitated gold nanowires and two electrodes mounted on aluminum oxide. Subsequent to the application of the suspension, the sample was subjected to a 2 h drying process in an oven set at a temperature of 100 °C.

2.3. Synthesis of C/TiO₂ Composite Fibers

The production of nanostructured composite fibers, incorporating PAN and CTP with the addition of titanium oxide nanoparticles, was successfully achieved. The preparation of the fiber-forming solution closely adhered to the methodology outlined in a previous section of this article. In brief, CTP was added to a 9% PAN:DMF solution with a PAN:CTP weight ratio of 7:3. Subsequently, titanium oxide nanoparticles were introduced, maintaining a (PAN/CTP):TiO₂ weight ratio of 7:3. The electroforming of fibers was carried out, followed by the processes of stabilization and carbonization. The samples obtained after carbonization were designated as "C/TiO₂ fibers".

The investigation of the photocatalytic performance of carbon nanofibers modified using titanium dioxide (C/TiO₂) was carried out through the photocatalytic degradation of methylene blue (MB). This degradation process occurred under the irradiation of a 300 W xenon lamp, with experiments conducted at room temperature. The lamp was positioned approximately 15–20 cm above the solution surface.

In the experimental procedure, 5 mg of C/TiO₂ were dispersed within a 50 mL solution of methylene blue, initially having a concentration of 10 mg/L. Following the introduction of the nanofibers, the mixed solution was allowed to stand in the dark and underwent stirring for 30 min to establish adsorption–desorption equilibrium within the system.

Subsequently, the entire system was placed under the xenon lamp to initiate the photocatalytic degradation process. At 10 min intervals, 5 mL aliquots of the solution were extracted and subjected to centrifugation. The purpose of this centrifugation step was to separate solid residues from the liquid phase for a further analysis.

2.4. Synthesis of C/Fe₃O₄ Composite Fibers

Magnetite (Fe₃O₄) nanoparticles were synthesized using a chemical condensation method as previously detailed in reference [50]. In brief, an aqueous solution of iron (III) chloride with a concentration of 0.32 mol/L and iron sulfate with a concentration of 0.2 mol/L was combined in a heat-resistant flask. This mixture was agitated using a heated magnetic stirrer, while a 25% aqueous ammonia solution was added gradually, at a rate of one drop per second. The temperature of the iron salt solution was maintained at 50 °C. Subsequently, magnetite nanoparticles were extracted from the solution using a permanent magnet, washed several times with water to neutralize the reaction, and then dried under standard conditions.

The fabrication of nanostructured composite fibers, incorporating PAN and CTP with the inclusion of magnetite nanoparticles, was successfully achieved. The preparation of the fiber-forming solution closely adhered to the procedure described in a previous section. In summary, CTP was incorporated into a 9% PAN/DMF solution with a PAN/CTP weight ratio of 7:3. Following this, magnetite nanoparticles were added, maintaining a PAN/CTP:Fe₃O₄ weight ratio of 7:3. Subsequently, the electroforming of fibers was conducted, followed by the crucial stages of stabilization and carbonization. The resulting samples were designated as “C/Fe₃O₄ fibers”.

2.5. Synthesis of C/AC Composite Fibers

The highly porous activated carbon (AC) was produced from rice husk waste, following the methodology detailed in a prior investigation [51]. The fabrication of composite fibers, incorporating PAN and CTP with the inclusion of activated carbon, was successfully carried out. The preparation of the fiber-forming solution closely adhered to the methods described in previous sections. In summary, CTP was introduced into a 9% PAN:DMF solution with a PAN:CTP weight ratio of 7:3. Subsequently, activated carbon was added, maintaining a (PAN/CTP):AC weight ratio of 7:3. Subsequently, the electroforming of fibers was performed, followed by the crucial stages of stabilization and carbonization. The samples obtained after carbonization were designated as “C/AC fibers”.

The sorption characteristics of the resulting C/AC composite fibers regarding the adsorption of manganese (II) ions from aqueous solutions were investigated with respect to adsorption time. Calibration solutions were carefully prepared to contain manganese (II) ions at concentrations of 5, 10, 15, and 20 mg/L, following the guidelines of State Standard, GSO (Certified Reference Material) no. 7875-2000. The working concentration was set at 10 mg/L. Samples of C/AC fibers, weighing 0.25 g, were immersed in 200 mL beakers filled with 100 mL of the working solution. At specific time intervals (3, 10, 30, 60, and 720 min), samples were retrieved from the beakers to determine the manganese ion content using atomic absorption spectrometry.

2.6. Methods of Characterization

2.6.1. X-ray Phase Analysis

X-ray patterns were obtained with a DRON-4 universal X-ray diffractometer equipped with an IBMPC-based digital control and registration system using copper radiation. This method allowed us to accurately determine the lattice parameters of crystalline materials and perform qualitative and quantitative phase analyses of materials. The X-ray tube operated at voltages up to 30 kV, with a tube current of 30 mA. The goniometer moved in steps of 0.05° 2θ, and the measuring point intensity reached up to 1.0. The sample's own-plane rotation speed was 60 rpm.

X-ray data were processed to determine angular position and reflection intensity using the 'Fpeak' program. The phase analysis was conducted through the 'PCPDFWIN' program, which utilized a diffractometric database. Spectra obtained were identified with reference to the JCPDS X-ray database. Notably, the primary hardware error in the X-ray counting measurement did not exceed 0.4%.

2.6.2. Electron Microscopy

The structure, size, and morphology of the obtained samples were investigated using a Quanta 200i 3D scanning electron microscope (FEI, Hillsboro, OR, USA) with an accelerating voltage of 30 kV. This microscopy analysis was carried out at the "National Nanotechnology Laboratory of Open Type" within KazNU (Al-Farabi University, Almaty, Kazakhstan). This method allowed us to determine surface structures in images, facilitating the assessment of both structural characteristics and the sizing of individual particles. Notably, the Quanta 200i 3D SEM is equipped with an energy-dispersive X-ray system (EDS), which enables the analysis of a wide range of chemical elements, spanning from B to U. The energy resolution of this system is 132 eV (Mn $K\alpha$).

In addition, the structural and morphological characteristics of magnetite nanoparticles were investigated using a transmission electron microscope, JEM-1011 (JEOL, Tokyo, Japan) in the Kazakhstan-Japan Innovation Center of the Kazakh National Agrarian Research University. This microscope is equipped with a digital camera, Morada (Olympus, Tokyo, Japan). Key technical specifications include an adjustable accelerating voltage within the range of 40 to 100 kV, a dot resolution of 0.3 nm, a line resolution of 0.14 nm, a LaB₆ electron gun, and a magnification range from 100 to 1,000,000.

Fiber diameters and particle sizes were determined from a set of SEM/TEM images using the open-source program "ImageJ", specially developed for an image analysis and processing, which automates the calculation of the average particle diameter and standard deviation.

2.6.3. Raman Spectroscopy

Raman spectra of the samples were obtained on an NT-MDT NTegra Spectra spectrometer located at the "National Nanotechnology Laboratory of Open Type" of KazNU (Al-Farabi University, Almaty, Kazakhstan).

Raman spectroscopy was carried out with unpolarized radiation from a semiconductor diode laser as the excitation source, emitting at a wavelength of $\lambda_{\text{exc}} = 473$ nm. The wavenumber scale had a relative error tolerance maintained within $\pm 0.5\%$.

2.6.4. P-45X Potentiostat-Galvanostat Workstation

The gas-sensitive properties were evaluated using a static test method. The sensor was positioned within a 10 L test chamber, with its electrodes connected to a P-45X potentiostat-galvanostat workstation. Current characteristics between the two electrodes were measured while exposing the sample to the analyzed gas. This procedure enabled the assessment of the composite fibers' sensitivity to gases when connected to the specialized microchip and measurement equipment.

A volume of vapor saturated with acetone was introduced into the chamber to create an environment with a specific concentration of acetone, and the gas detection characteristics of the sensor were recorded. The sensor response was determined using the following Formula (1):

$$R = (I_a - I_g) / I_g, \quad (1)$$

where I_a is the sensor current in air; I_g is the sensor current in the acetone environment.

2.6.5. UV-Vis Spectroscopy

The UV-Vis absorption spectrum of the material is to analyze the change in UV-Vis spectra of methylene blue solutions before and after the photocatalytic degradation process after centrifugation.

The analysis was conducted using a UV-Vis spectrophotometer, enabling us to quantify the amount of methylene blue adsorbed using the material based on the observed spectral changes.

This technique provided valuable insights into the adsorption capacity and efficiency of the test material for methylene blue molecules. The spectral analysis yielded essential data concerning the degradation efficiency of methylene blue over time, facilitating an evaluation of the photocatalytic activities of the C/TiO₂.

2.6.6. Atomic Absorption Spectroscopy

Atomic absorption spectroscopy was used to evaluate the adsorption capacity of the obtained materials on metal ions. Alterations in the concentration of manganese ions in acidified aqueous solutions were analyzed using atomic absorption spectra, utilizing a “PerkinElmer AAnalyst 200” instrument. Sample concentrations were determined by introducing the sample into the flame of an acetylene-air burner as a nebulizer. The margin of error associated with the experiment was within $\pm 2.5\%$.

$$a = \frac{(C_0 - C) \cdot V}{g}, \quad (2)$$

where C_0 and C are concentrations of metal ions in the solution before and after precipitation, mg/L; V is the volume of the solution, L; g is the mass of the composite fibers, g.

3. Results and Discussion

3.1. Characterization of Coal Tar Pitches Obtained with Thermal Treatment

The coal tar used in this study was sourced from the Shubrakol coal deposit in Kazakhstan. The Shubrakol field holds substantial reserves, amounting to an impressive 1.5 billion tons. Coal tar itself is characterized as a dense, dark liquid with a distinctive odor, exhibiting a viscosity of 1.04 g/cm³.

To examine the properties of coal tar, specimens were subjected to controlled heating processes at various temperature intervals, and the mass variation was meticulously assessed by comparing the pre- and post-treatment weights of the samples. The resulting data is summarized in Figure 2, providing insights into the extent of mass reduction following each treatment. As indicated in the tabulated data in Figure 2, the peak of mass reduction occurs at the temperature threshold of 500 °C, representing approximately 76% of the initial mass. The application of thermal treatment accelerates the elimination of volatile constituents within the coal tar substrate.

The data presented on the heat treatment of coal tar are instructive in understanding its chemical transformation with increasing temperature. The significant mass loss observed at 500 °C indicates the substantial removal of volatile fractions. This is crucial for materials intended for further high-temperature applications, such as carbonization. The removal of sulfur from the composition at 400 °C is particularly significant. Sulfur can be undesirable in carbon materials as it leads to impurities and can affect the final properties of carbon-based materials.

The reduction in volatile content and the removal of sulfur at higher temperatures enhance the carbonization potential of the material, which is favorable for the production of high-quality carbon materials. The removal of volatile components implies greater structural stability at elevated temperatures, which is beneficial for applications requiring thermal resistance.

The analysis of SEM imagery reveals significant structural alterations in coal tar samples subjected to varying processing temperatures. At an initial processing temperature of 200–250 °C, discernible transformations manifest in the form of a porous microstructure and the initiation of active mesophase centers. Subsequent elevation of the processing temperature to 300 °C results in a pronounced escalation in surface degradation. The treated sample exhibits a more pronounced topographical relief, accompanied with a heightened density of mesophase centers per unit area. At a processing temperature of

350 °C, a critical transition is observed, marking the shift from an isotropic to an anisotropic structural configuration. Notably, this sample demonstrates the complete removal of volatile fractions, yielding a homogeneous surface with mesophase centers averaging around 2 µm in size.

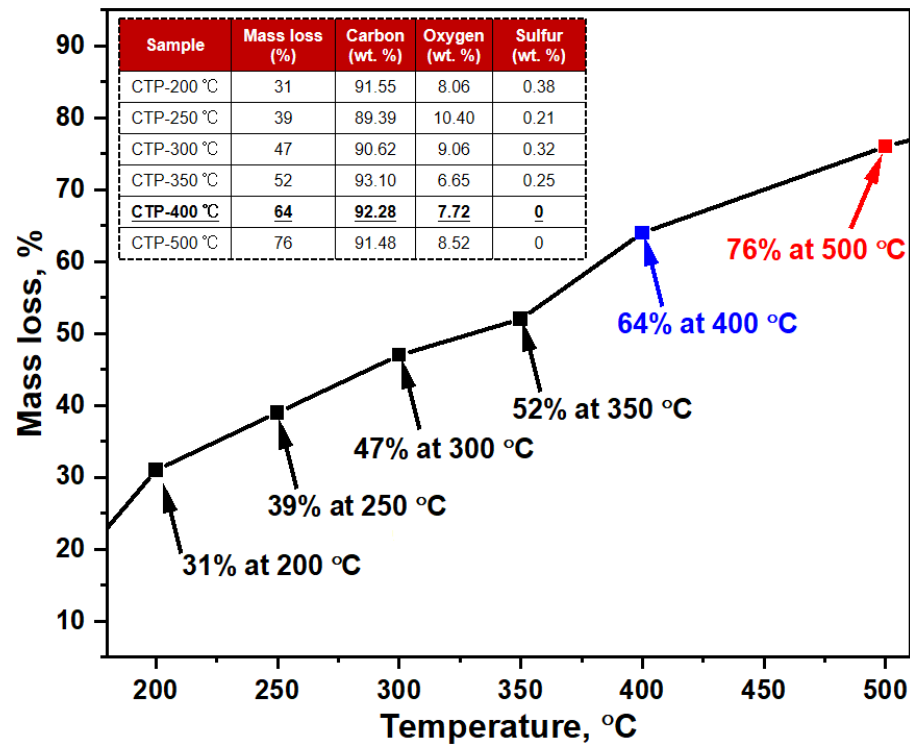


Figure 2. Mass loss and elemental composition of coal tar after heat treatment.

When coal tar is processed at 400 °C, a comparable anisotropic structure forms, occasionally featuring a layered arrangement. This structural alteration accompanies an increased degree of graphitization within the sample. The size of the mesophase particles notably expands to a range of 3.5–5 µm. The culmination of this temperature-based experimentation occurs at a coal tar processing temperature of 500 °C, resulting in a definitive transition from an isotropic to an anisotropic structural state.

Figure 3 shows the Raman spectra obtained from coal tar subjected to different temperature treatments. The interpretation of these Raman spectra was carried out with reference to the comprehensive analysis presented in research article [52].

In the context of the original graphite, two primary first-order peaks manifest themselves at wavenumbers of 1355 cm⁻¹ (referred to as the D peak, associated with the defective Raman zone) and 1575–1582 cm⁻¹ (referred to as the G peak, attributed to the presence of carbon atoms in the sp² state and located within the graphite lattice plane). In particular, the second-order spectral lines around ~2710 cm⁻¹ show minimal resolution and considerable disorder, making their identification impossible. Several key parameters are crucial in interpreting Raman spectra: λ_D and λ_G, the wavenumbers of the D and G peaks, respectively, measured in cm⁻¹; I_D and I_G, the intensities of the D and G peaks in relative units; and R, the ratio of the intensities of the D and G peaks (I_D/I_G). The appearance of graphite nanocrystallites in the sample is accompanied with a shift of the G peak from 1575–1582 cm⁻¹ to higher values, around ~1600 cm⁻¹. Accurate interpretation of peak half-width and area requires careful determination of the background line in the Raman spectrum.

Within the samples designated CTP-200, CTP-250, and CTP-300, there is an observable shift of the G-peak towards higher frequencies, approximately in the range of ~1405–1428 cm⁻¹. This phenomenon can be attributed to the presence of clusters with a

reduced number of aromatic rings in these samples. In particular, there is considerable background noise in these two samples, which makes it difficult to accurately determine the degree of graphitization. Consequently, the R value, indicating the I_D/I_G ratio, has not been considered for these samples. A brief summary of the wavelengths of the G and D peaks, their corresponding intensities, and R values are given in Table 1.

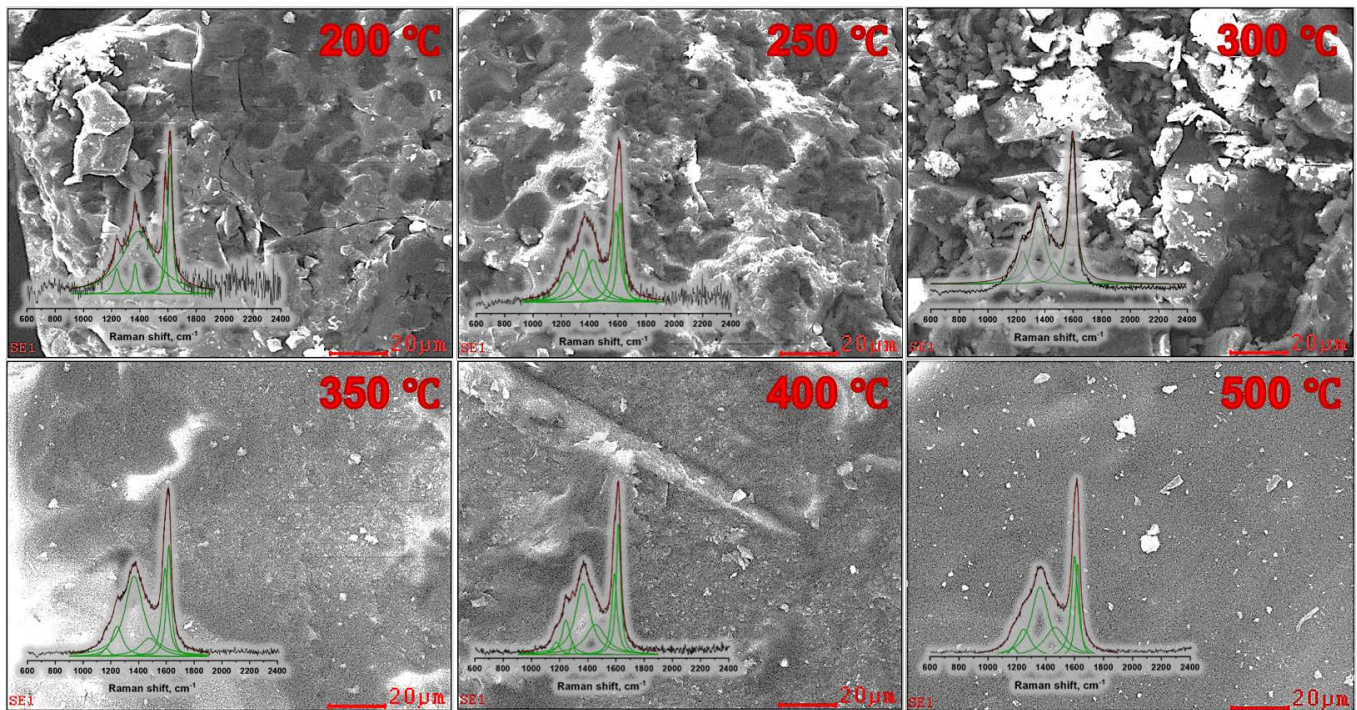


Figure 3. SEM images (with Raman shifts) of coal tar after heat treatment.

Table 1. Characteristics of G and D peaks for coal tar samples treated at different temperatures.

Sample	$\lambda_D, \text{cm}^{-1}$	$\lambda_G, \text{cm}^{-1}$	I_D	I_G	R (I_D/I_G)
CTP-200 °C	1428	1610	736	938	-
CTP-250 °C	1417	1607	754	980	-
CTP-300 °C	1405	1603	791	1041	-
CTP-350 °C	1356	1600	1102	1605	0.6866
CTP-400 °C	1363	1610	394	639	0.7214
CTP-500 °C	1356	1606	392	604	0.6490

For sample CTP-350, a significant change in both the intensities and positions of the G and D peaks can be seen. This change implies the elimination of all volatile fractions and the onset of a transition from a disordered to a more ordered structural state, characterized by the formation of mesophase centers. Additionally, for samples CTP-350, CTP-400, and CTP-500, an observable shift of the D peak towards the region of 1600–1610 cm^{-1} is noted, which can be attributed to the appearance of nanocrystalline mesophase centers.

Based on the data presented in Table 1, it is possible to estimate the degree of graphitization using the equation provided [53]:

$$g(\%) = \left[1 - \frac{R}{n} \right] \cdot 100 \quad (3)$$

where g is the graphitization degree, %; R is the I_D/I_G ratio; n is the maximum value of R obtained during the study (in this case, 0.7214).

Thus, the calculation showed that for sample CTP-350, the degree of graphitization is ~5%; for sample CTP-500, it is ~10%. For sample CTP-400, this indicator cannot be determined, because the value of R was taken as the maximum value (n).

3.2. Characterization of C/NiO Composite Fibers

Within the X-ray diffraction pattern (Figure 4), there are four noticeable peaks. These peaks are distinctly located at 2θ angles of 37.27° , 43.27° , 62.84° , and 75.42° . Importantly, they correspond to cubic NiO crystalline structures, with each peak originating from a distinct diffraction plane: (111), (200), (220), and (311), respectively. It is worth noting that these diffraction peaks closely match the expected pattern defined in the JCPDS card 47-1049. Consequently, the XRD data strongly suggest that the sample primarily comprises single-phase nickel oxide. The size of the nickel oxide crystallites, estimated using the Scherrer equation, approximates 480 \AA .

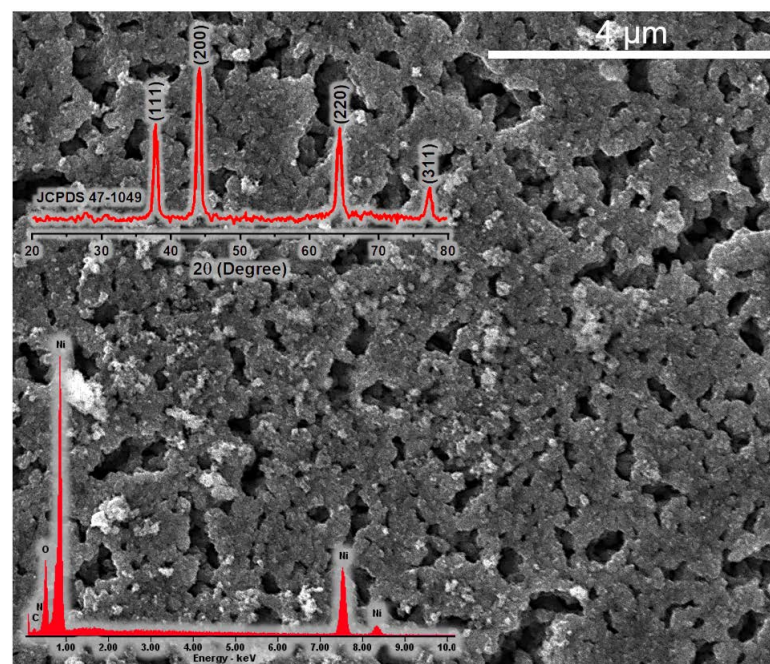


Figure 4. SEM (with EDAX-analysis and XRD pattern) image of NiO nanoparticles.

The SEM analysis (Figure 4) shows that the nanoparticles exhibit a spherical morphology and, notably, tend to form agglomerates. This aggregation phenomenon is likely driven by the nanoscale dimensions of the crystallites and the presence of numerous uncompensated surface bonds. The inherent high surface energy associated with nanocrystals compels them to aggregate, a mechanism aimed at minimizing surface energy during the synthesis process.

Furthermore, the specific surface area of the NiO nanoparticles has been determined to be $65.544 \text{ m}^2/\text{g}$, which is a promising outcome for oxide materials. In comparison, a previous study conducted by the authors [54] involved the synthesis of nickel oxide through the sol-gel method, yielding a significantly lower specific surface area of $5.8 \text{ m}^2/\text{g}$. This comparison underscores that nickel oxide produced via the solution combustion method exhibits reduced dimensionality and heightened porosity, making it a noteworthy advancement in materials synthesis.

PAN/CTP/NiO composite fibers were fabricated via the electrospinning technique, subsequently of stabilization and carbonization processes. In Figure 5, depiction is presented, encompassing both the SEM image and the accompanying diameter distribution analysis of the electrospun composite fibers following the stages of stabilization and carbonization.

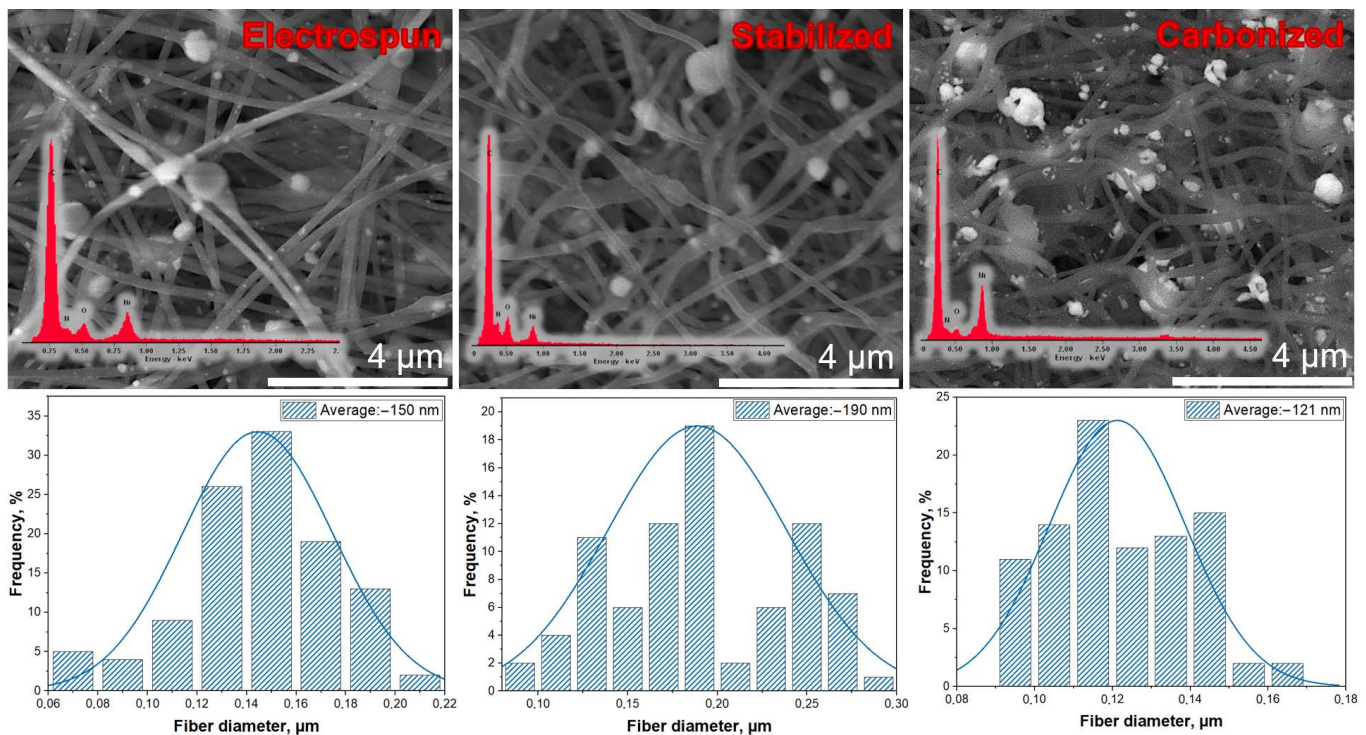


Figure 5. SEM (with EDAX-analysis) image and fiber distribution of PAN/CTP/NiO fibers after electrospinning, stabilization, and carbonization processes.

Fibers produced via the electrospinning method exhibit structural resilience during subsequent heat treatment processes, including stabilization and carbonization. These critical steps, involving high temperatures and chemical transformations, do not compromise the integrity of the electrospun fibers. This retention of structure is vital for the practical applications.

SEM images illustrate the successful inclusion of nickel nanoparticles within the fiber structure. Additionally, these images reveal the formation of visible agglomerates on the fiber surface. NiO particles have high adhesion to the fiber surface due to chemical and physical changes occurring during the carbonization process.

The alteration of average fiber diameter throughout the fabrication process, from electrospinning (150 nm) to stabilization (190 nm) and finally to carbonization (121 nm), can be attributed to several factors. During stabilization, elevated temperatures cause some swelling due to cross-linking and the elimination of volatile components. Subsequently, carbonization results in a reduction in diameter due to the removal of non-carbon atoms and the development of a denser, graphitic carbon structure. This dynamic process allows for precise control over fiber diameter and, consequently, material properties for various applications.

To determine the optimal operating temperature for the composite fibers, an investigation was conducted into the influence of heating temperature on the response of these fibers when exposed to 100 ppm of the test gas, namely acetone (as depicted in Figure 6). Observations reveal a nuanced temperature-dependent response pattern. As the temperature escalates from 160 °C, the sensor response exhibits a gradual increase, culminating at its zenith around 220 °C, only to exhibit a rapid decline with further temperature elevation. This observed behavior primarily hinges on the temperature's impact on the adsorbed gas.

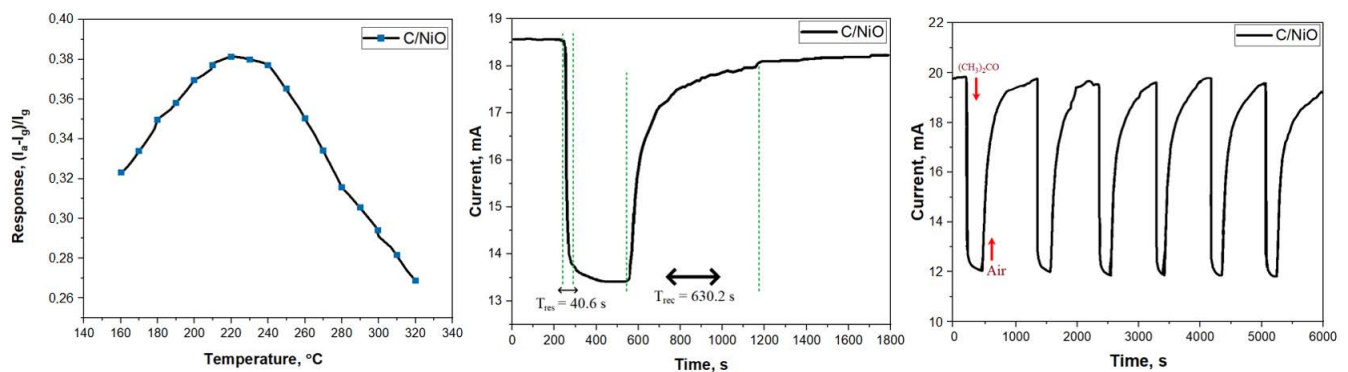


Figure 6. Graph of resistance dependence on operating temperature (a), response and recovery time (b), and operating time (c) for C/NiO-based gas-sensing material for acetone/air mixture.

In ambient air, oxygen molecules are adsorbed onto the surface of the sensing material. As the temperature rises, a transition occurs from physical adsorption to chemical adsorption for the adsorbed gas. Notably, oxygen ions, which facilitate electron transfer within the adsorbed gas, can significantly amplify the reaction within a specific temperature range. However, if the temperature exceeds a certain threshold, it can impede the adsorption of gas onto the sensing material's surface.

Figure 6 illustrates the composite fibers' response to 100 ppm of acetone at the optimal operating temperature. Upon introduction of gaseous acetone into the test chamber, the sensor current value exhibits a rapid decrease, swiftly followed by an increase in sensor current upon the cessation of acetone exposure.

Both microdispersed and nanodispersed nickel oxide particles are recognized for their gas-sensitive properties, yet their sensitivity and response times to gas exposure may diverge. Generally, nanodispersed nickel oxide particles boast a larger surface area in comparison to their microdispersed counterparts, endowing them with a heightened capacity for detecting and responding to gas exposure [55]. This advantage translates to faster response times and greater sensitivity. Nevertheless, it is worth noting that a precise comparison between the two is contingent on factors such as particle size, morphology, distribution, and the specific gas under consideration [56]. The response of the optimized sensor is compared with those of previously reported ones in Table 2, demonstrating that the as-fabricated gas sensor exhibits superior acetone sensing performances.

Table 2. Comparison of NiO-based gas sensors.

Sensor	Conc. (ppm)	T (°C)	Res. Time (s)	Ref.
Rh–NiO nanofibers	200	225	134	[57]
In ₂ O ₃ –NiO nanofibers	50	260	20	[58]
NiO sphere	200	290	25	[59]
NiO–ZnO sphere	200	260	8	[59]
NiO nanofibers	100	180	127	[60]
C/NiO fibers	100	220	40.6	This study

In essence, the superior surface-area-to-volume ratio inherent to nanodispersed nickel oxide particles engenders enhanced surface reactivity and heightened sensitivity to fluctuations in gas concentration [61]. This heightened sensitivity emerges from the greater abundance of active sites available for interaction with gas molecules [62]. Additionally, the diminutive size of nanodispersed nickel oxide particles accelerates the diffusion of gas molecules towards these active sites, thereby contributing to swifter response times.

Conversely, microdispersed nickel oxide particles typically exhibit smaller surface areas, resulting in lower sensitivity to variations in gas concentration. Nevertheless, their utility in gas detection remains valuable due to factors such as cost-effectiveness, stability, and ease of synthesis when compared to their nanodispersed counterparts.

It is imperative to acknowledge that the gas sensing characteristics of microdispersed and nanodispersed nickel oxide particles can exhibit substantial variations contingent upon numerous factors, including particle size, morphology, crystal structure, surface chemistry, and the presence of impurities or surface defects. Consequently, a comprehensive analysis of the gas-sensitive attributes of both forms of nickel oxide is requisite for a definitive comparison.

According to the operating principle of p-type semiconductors such as NiO, oxygen molecules adsorbed onto the surface capture electrons from the semiconductor, transforming into ionic species in the presence of air [63]. This transformation results in an augmentation of basic carriers, thereby yielding high sensor current values in ambient air. However, gaseous acetone, being a reducing gas, initiates a reaction between the reducing gas and oxygen ions on the NiO surface when exposed to the sensor. Based on our findings, the response and recovery times for NiO amount to 40.6 s and 630.2 s, respectively.

3.3. Characterization of Obtained C/TiO₂ Composite Fibers

Composite fibers were synthesized through the incorporation of titanium oxide nanoparticles into a matrix comprising polyacrylonitrile and coal tar pitch. The morphological characteristics of these fibers after stabilization and carbonization were studied using SEM (Figure 7). SEM images demonstrate the preservation of the fibrous structure, which is emphasized with the presence of crystalline inclusions of metallic nanoparticles adhering to the fiber face, as well as the formation of nanoparticle agglomerates.

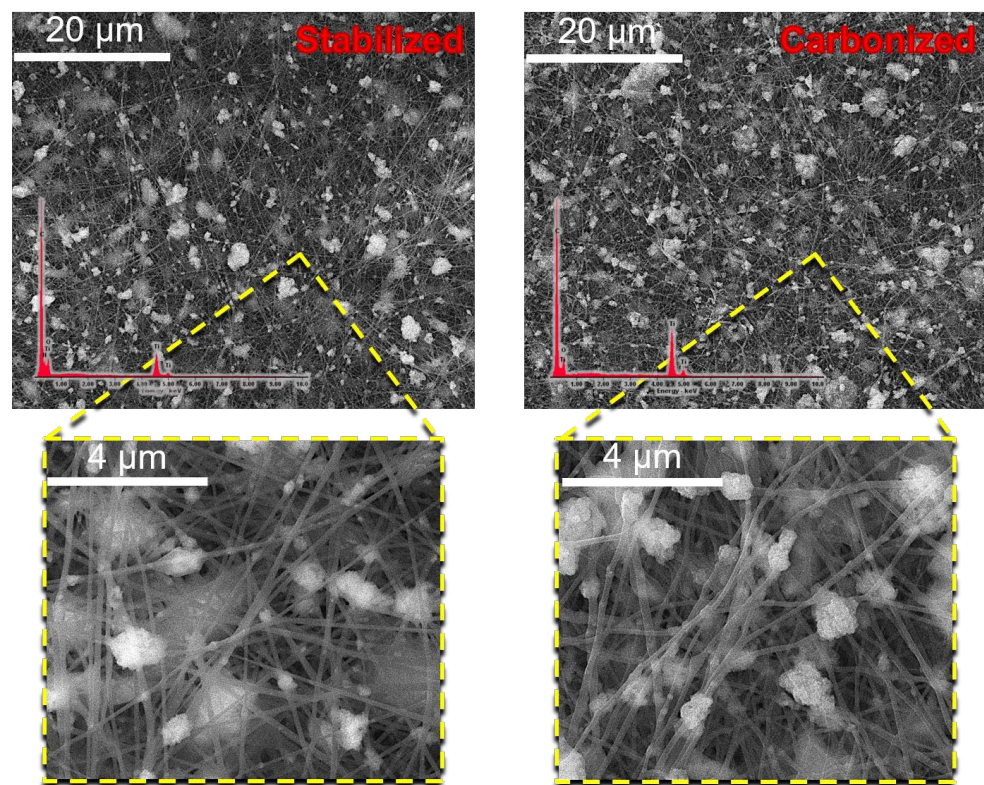


Figure 7. SEM images of composite fibers PAN/CTP/TiO₂ after stabilization and carbonization.

Figure 8 shows the change in the concentration of methylene blue during the adsorption process in the absence of light. Here, C_0 is the initial concentration of the dye, while C_t is the remaining concentration of MB at that time.

The degradation efficiency $D\%$ is obtained with the following equation:

$$D \% = C_0 - C_t / C_0 \times 100\%, \quad (4)$$

where C_0 is the concentration of MB. The final degradation efficiency is obtained by taking the C_t value when t is 180 min. It is seen that the degradation efficiency is about $96.13 \pm 0.05\%$, which is the highest efficiency.

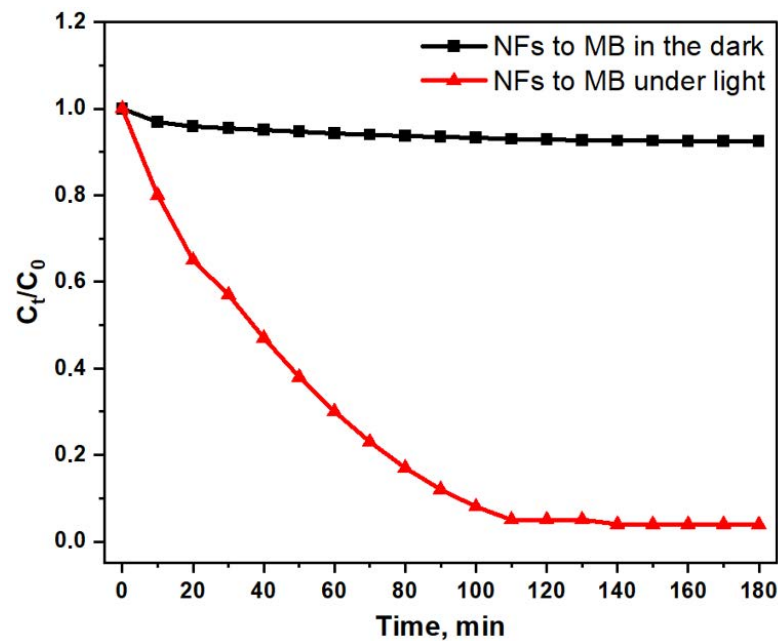


Figure 8. The adsorption profile of C/TiO₂ to MB in the dark and under light.

Table 3 provides a comparison of different photocatalysts in their ability to degrade specific model dye pollutants, along with the degradation rates and irradiation times. The last entry is for the current study.

Table 3. Comparison of TiO₂-based photocatalysts.

Photocatalyst	Model Dye Pollutant	Degradation Rate	Irradiation Time (min)	Ref.
Fe/TiO ₂ fibers	RhB	99	120	[64]
C/TiO ₂ fibers	MB	97.7	120	[65]
CFs/TiO ₂ seed-layer/TiO ₂ nanorods	MB	96.7	80	[66]
TiO ₂ -CFs	RhB	60	40	[67]
C/TiO ₂ fibers	MB	96.13	180	This study

The obtained results are of practical interest for the removal of organic dyes using photocatalytic decomposition, as demonstrated with the example of methylene blue decomposition. The results indicate that C/TiO₂ composite fibers were obtained after stabilization and carbonization of PAN/CTP/TiO₂ fibers. These fibers after high-temperature treatment and removal of all volatile components possess both chemical stability and mechanical strength [68].

The structure of the resulting fibers resembles a “beads-on-a-string” [69] configuration, where the “beads” are crystalline TiO₂ inclusions interconnected with carbon fibers. This structure provides access to photocatalytically active TiO₂ for the degradation of dye molecules such as MB. Since the mat composed of C/TiO₂ fibers can be approximated as a permeable membrane due to the voids between the fibers, even TiO₂ particles in the deeper layers of the electrospun mat remain active [70]. These results are promising for the application of composite fibers in photocatalytic processes, especially in areas such as wastewater treatment and environmental protection.

3.4. Characterization of C/Fe₃O₄ Composite Fibers

The examination of magnetite nanoparticles involved a comprehensive investigation utilizing XRD and TEM. In Figure 9, the TEM image with the particle size distribution is presented based on the TEM analysis of the magnetite particles synthesized via chemical deposition. Predominantly, the particles fell within the size range of 6 to 16 nm, with an average particle diameter measuring approximately 12.22 nm.

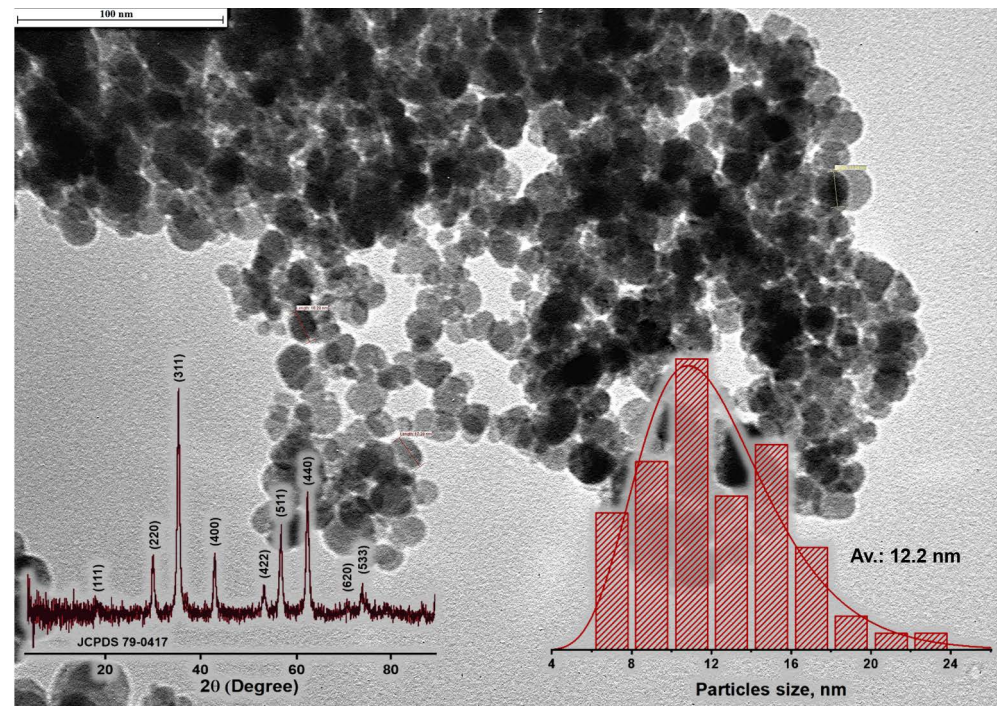


Figure 9. TEM image (with particle size distribution and XRD patterns) of magnetite nanoparticles.

The X-ray pattern of the magnetite nanoparticles, as illustrated in Figure 9, reveals a distinctive pattern marked by nine well-defined diffraction peaks occurring at 2θ angles of 18.5, 30.1, 35.5, 43.2, 53.6, 57.1, 62.7, 71.3, and 74.2 degrees. These angles correspond precisely to the crystallographic planes of the magnetite phase, specifically identified as (111), (220), (311), (400), (422), (511), (440), (620), and (533), respectively (JCPDS card 03-065-3107).

The average particle size, symbolized as ‘ t ’, was calculated employing the Scherrer equation, $t = \lambda / (\beta \cos \theta)$. In our analysis, the size of the synthesized magnetite particles was conclusively determined to be 10.4 nm, a result that consistently concurs with the data obtained from TEM imaging.

The morphology of the obtained fibres was examined by SEM (Figure 10). The elemental analysis of electrospun PAN/CTP/Fe₃O₄ fibers yielded the following compositional data:

In the electrospun state, carbon (C) constituted 65.95 wt.%, nitrogen (N) comprised 17.49 wt.%, oxygen (O) constituted 7.23 wt.%, and iron (Fe) accounted for 9.33 wt.%.

Post-stabilization, the composition exhibited slight variations, with carbon at 65.86 wt.%, nitrogen at 17.63 wt.%, oxygen at 6.96 wt.%, and iron at 9.55 wt.%.

Following carbonization, a pronounced transformation was observed, with carbon content reducing substantially to 41.50 wt.%, nitrogen diminishing to 3.01 wt.%, oxygen increasing to 15.25 wt.%, and iron markedly escalating to 40.06 wt.%.

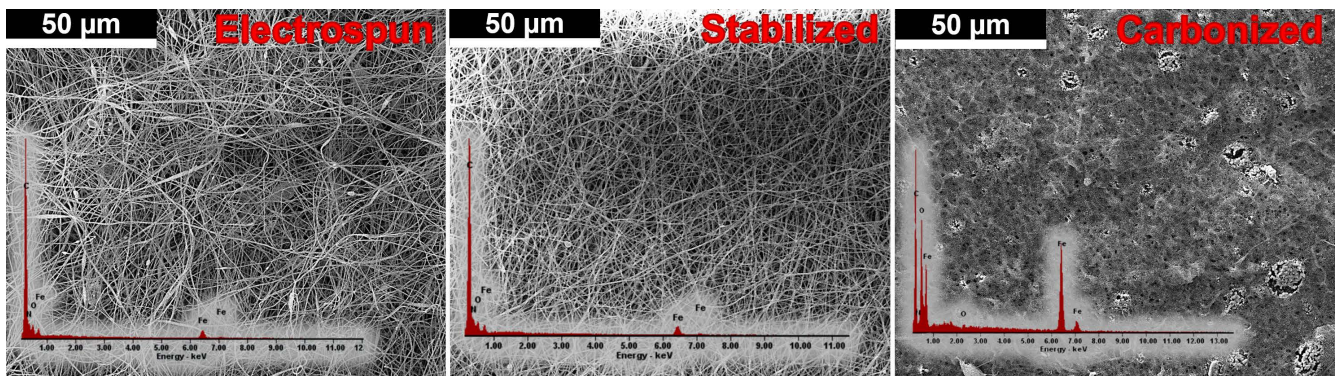


Figure 10. SEM images (with EDAX-analysis) of electrospun, stabilized, and carbonized PAN/CTP/Fe₃O₄ composite fibers.

Changes in the elemental composition of PAN/CTP/Fe₃O₄ fibers during the stabilization and carbonization processes can be explained with the main processes occurring at each stage. Initially, the primary constituents of the fibers were carbon, nitrogen, oxygen, and iron, reflecting the composition of the starting materials. During the stabilization stage, there was a loss of carbon and slight changes in nitrogen content, while the iron content remained constant. Subsequently, during the carbonization process, there was a decrease in carbon and nitrogen content, and the increased presence of iron was attributed to its concentration in the remaining material. In general, the changes in the content and composition of C/Fe₃O₄ fibers at different stages are related to the chemical and structural transformations that occur during processing. The processes of stabilization and carbonization lead to the removal of organic components and their transformation into carbon structures [71], which explains the variations in the content of carbon, nitrogen, oxygen, and iron at each stage.

In summation, the variations in mass content and elemental composition observed at distinct phases of C/Fe₃O₄ fiber production are fundamentally a consequence of the intricate chemical and structural metamorphoses occurring during the heating and processing of the fibers. The stabilization and carbonization processes are marked by the removal of organic components and the conversion of precursor fibers into carbon-enriched structures, thereby accounting for the marked fluctuations in carbon, nitrogen, oxygen, and iron content observed at each juncture.

3.5. Characterization of C/AC Composite Fibers

3.5.1. Characterization of Activated Carbon Obtained from Rice Husk

Composite fibers based on polyacrylonitrile and coal tar pitches with the addition of activated carbon particles synthesized from rice husk, a vegetable waste, were obtained. As can be seen from the results of the SEM analysis (Figure 11), the sample has a loose-layered structure with a texture of pores represented by interconnected cavities formed because of the release of volatile organic substances.

Activated carbon due to its large surface area and porous architecture, providing exceptional adsorption, adsorbs heavy metal ions, promoting their removal from aqueous solutions [21]. This is facilitated with numerous active sites within activated carbon that bind heavy metal ions through mechanisms such as ion exchange and chemical adsorption [22]. Consequently, using activated carbon declines heavy metal ion concentration in water, promoting water safety and environmental preservation. Furthermore, the adoption of activated carbon in removing heavy metal ions can enhance wastewater quality and prevent soil and groundwater contamination, making it vital for water treatment and environmental protection.

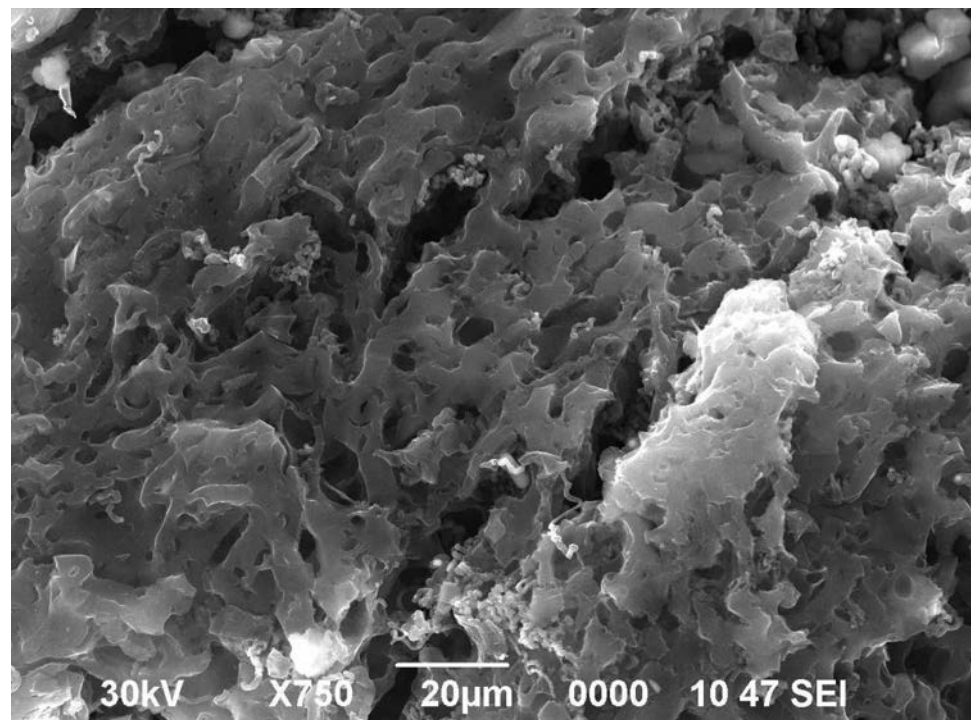


Figure 11. SEM image of activated carbon.

3.5.2. Characterization of PAN/CTP/AC Fibers

In an analytical context, examination of SEM images, depicted in Figure 12, regarding composite fibers based on PAN/CTP/AC, revealed an absence of a methodical orientation axis during spinning. Rather, these fibers displayed a random and disorganized arrangement. After undergoing thermal treatments that included both stabilization and carbonization processes, a notable observation was made: the fibrous structure was preserved without any evident defects or dislocations. This indicates that the fibers maintained their resilience and structural integrity throughout the heat treatment regimen. Upon a thorough examination of micrographs at varying magnifications, a consistent dispersion of the fibers was observed. The uniform distribution remained consistent across various magnifications, demonstrating homogeneous fiber morphology throughout the range under examination. Furthermore, the analysis of fiber shape confirmed the uniformity and homogeneity of the fibers.

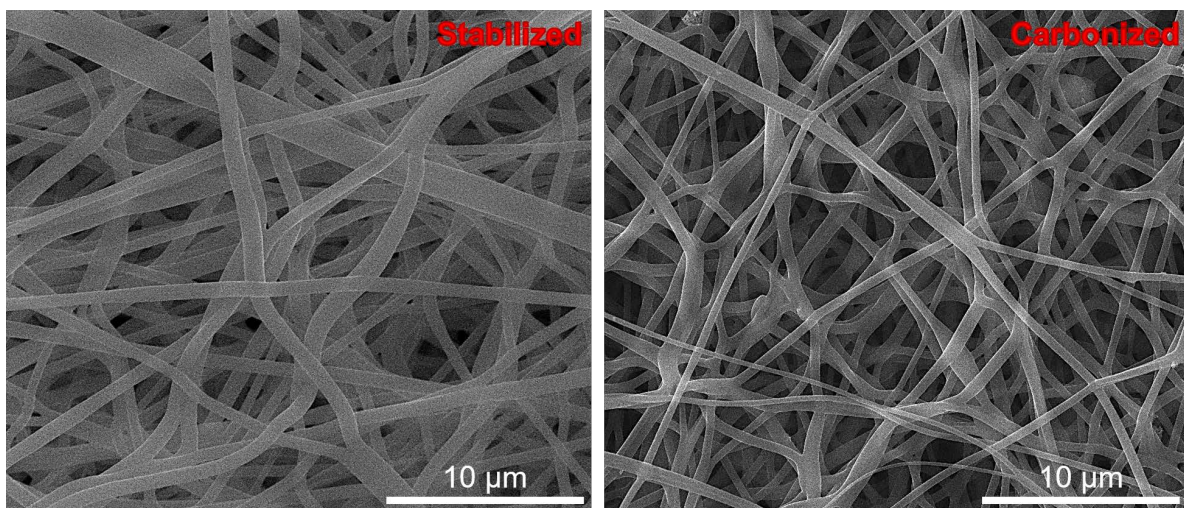


Figure 12. SEM images of PAN/CTP/AC fibers after stabilization and carbonization.

There is a reduction in fiber diameter after carbonization owing to different factors. PAN undergoes thermal decomposition during carbonization, leading to the elimination of non-carbonaceous components in the form of volatile gases like water vapor, carbon dioxide, and ammonia [72]. This procedure enhances carbon content within the fibers. As the atomic radius of carbon atoms is smaller compared to heteroatoms present in PAN [73], the carbon structure undergoes rearrangement, leading to increased order, shrinkage, and densification, ultimately decreasing their diameter. The precise and consistent fiber measurements, with an average diameter of 0.5 μm , were demonstrated.

3.5.3. Investigation of Metal Ion Sorption Properties

Composite fibers with activated carbon are used in water purification to eliminate heavy metal ions [21,22,74–81]. The collaboration of the fiber matrix in the composite material and the large surface area of the activated carbon enhances the removal of heavy metal ions from water due to its sorption properties. The fibrous matrix increases the contact area of water with the sorbent, while the activated carbon particles act as potent sorption centers for heavy metal ions. Empirical research has confirmed that these fibers possess a high sorption capacity towards heavy metal ions like lead [82], cadmium [83], and mercury [83,84], attributed to the activated carbon's large surface area and porous structure. A comprehensive analysis was conducted on the sorption properties of the composite fibers obtained (refer to Figure 13) during the adsorption process of manganese (II) ions from water at various time intervals. This study will present insights into the kinetics and efficiency of adsorbing manganese (II) ions through composite fibers.

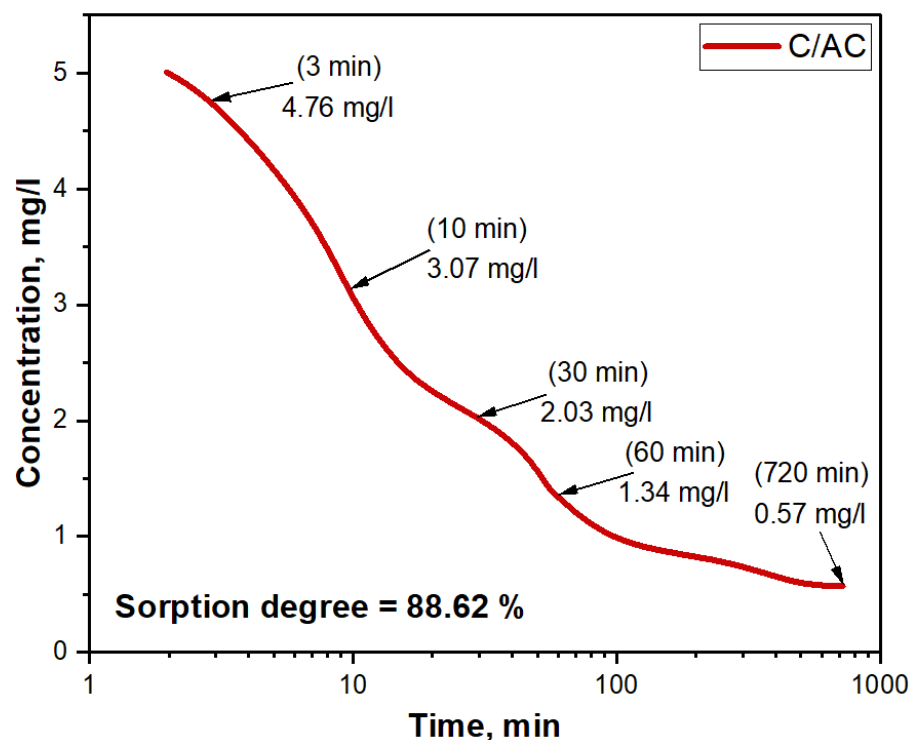


Figure 13. Sorption of manganese (II) ions of ISO 7875-2000 in aqueous solution using C/AC composite fibers at different times.

Table 4 presents a comparative analysis of diverse carbon-based sorbents for their efficiency in eliminating manganese from aqueous solutions. The analysis includes data on the percentage of manganese removal, initial concentration, and operating temperature. The final entry pertains to the current study.

Table 4. Comparison of carbon-based sorbents.

Carbon-Based Sorbent	Manganese Removal (%)	Initial Concentration (mg/L)	T (°C)	Ref.
Rice husk ash	100	3.8	30	[85]
PVA/chitosan	84.5	20	30	[86]
White rice husk ash	26.6	100	34	[87]
Untreated banana peel	80	10	25	[88]
C/AC fibers	88.62	5	25	This study

4. Conclusions

The research results encompass the synthesis and testing of composite electrospun fibers using coal tar pitch and various nanomaterial additives for eco-bio-applications. The thermal treatment of coal tar has unveiled its environmental potential, as high temperatures remove volatile components and sulfur, rendering it suitable for fiber electrospinning and subsequent carbonization. The successful application of CTP as an additive to a basic PAN solution is demonstrated through the synthesis of composite fibers incorporating CTP and nanomaterials like nickel oxide (NiO), titanium dioxide (TiO₂), and activated carbon (AC). NiO nanoparticles were obtained through the solution combustion method, while activated carbon was synthesized from agricultural waste, specifically rice husks. The C/NiO fibers exhibited good sensitivity to 100 ppm acetone at 220 °C with a response time of 40.6 s. The C/TiO₂ fibers, resembling a “beads-on-a-string” structure, demonstrated a high efficiency of 96.13% in the decomposition of methylene blue. Additionally, the C/AC fibers exhibited good adsorption characteristics, as evidenced with their efficient sorption of manganese (II) ions in aqueous solutions, with an efficiency of 88.62%. This research showcases how a combination of various methods, approaches, and materials, including waste materials, can lead to the production of composite materials with a broad range of applications. Beyond advancing the field of composite materials science, this work paves the way for sustainable solutions to pressing eco-bio-challenges. The developed composite fibers exemplify the potential of environmentally responsible materials and technologies to contribute to a greener and more sustainable future.

Author Contributions: All authors contributed to the study conception and design. Material preparation, data collection, and analysis were performed by B.K., G.S., A.I. (Aigerim Imash), A.I. (Akram Ilyanov) and Z.M. The first draft of the manuscript was written by B.K. and all authors commented on previous versions of the manuscript. All authors have read and agreed to the published version of the manuscript.

Funding: This research was funded by The Ministry of Science and Higher Education of the Republic of Kazakhstan, grant number: AP09259842.

Institutional Review Board Statement: Not applicable.

Informed Consent Statement: Not applicable.

Data Availability Statement: The data presented in this study are available within the article.

Conflicts of Interest: The authors declare no conflict of interest.

References

- Ahmad, F.; Saeed, Q.; Shah, S.M.U.; Gondal, M.A.; Mumtaz, S. Environmental Sustainability: Challenges and Approaches. In *Natural Resources Conservation and Advances for Sustainability*; Elsevier: Amsterdam, The Netherlands, 2022; pp. 243–270. [\[CrossRef\]](#)
- Aithal, S.; Aithal, P.S. Green Nanotechnology Innovations to Realize UN Sustainable Development Goals 2030. *Int. J. Appl. Eng. Manag. Lett.* **2021**, *5*, 96–105. [\[CrossRef\]](#)
- Frenot, A.; Chronakis, I.S. Polymer Nanofibers Assembled by Electrospinning. *Curr. Opin. Colloid Interface Sci.* **2003**, *8*, 64–75. [\[CrossRef\]](#)

4. Farshchi, R.; Ramsteiner, M. Spin Injection from Heusler Alloys into Semiconductors: A Materials Perspective. *J. Appl. Phys.* **2013**, *113*, 191101. [\[CrossRef\]](#)
5. Thejas Prasannakumar, A.; Mohan, R.R.; Varma, S.J. Progress in Conducting Polymer-Based Electrospun Fibers for Supercapacitor Applications: A Review. *ChemistrySelect* **2023**, *8*, e202203564. [\[CrossRef\]](#)
6. Langwald, S.V.; Ehrmann, A.; Sabantina, L. Measuring Physical Properties of Electrospun Nanofiber Mats for Different Bio-medical Applications. *Membranes* **2023**, *13*, 488. [\[CrossRef\]](#) [\[PubMed\]](#)
7. Lv, H.; Liu, Y.; Bai, Y.; Shi, H.; Zhou, W.; Chen, Y.; Liu, Y.; Yu, D.-G. Recent Combinations of Electrospinning with Photocatalytic Technology for Treating Polluted Water. *Catalysts* **2023**, *13*, 758. [\[CrossRef\]](#)
8. Wang, M.-L.; Yu, D.-G.; Bligh, S.W.A. Progress in Preparing Electrospun Janus Fibers and Their Applications. *Appl. Mater. Today* **2023**, *31*, 101766. [\[CrossRef\]](#)
9. Wang, P.; Lv, H.; Cao, X.; Liu, Y.; Yu, D.-G. Recent Progress of the Preparation and Application of Electrospun Porous Nanofibers. *Polymers* **2023**, *15*, 921. [\[CrossRef\]](#)
10. Zoppas, F.M.; Beltrame, T.F.; Sosa, F.A.; Bernardes, A.M.; Miró, E.; Marchesini, F.A. Superficial properties of activated carbon fiber catalysts produced by green synthesis and their application in water purification. *Environ. Sci. Pollut. Res.* **2020**, *27*, 40405–40420. [\[CrossRef\]](#)
11. Ji, W.; Wang, X.; Ding, T.; Chakir, S.; Xu, Y.; Huang, X.; Wang, H. Electrospinning preparation of nylon-6@UiO-66-NH₂ fiber membrane for selective adsorption enhanced photocatalysis reduction of Cr(VI) in water. *Chem. Eng. J.* **2023**, *451*, 138973. [\[CrossRef\]](#)
12. Mamah, S.C.; Goh, P.S.; Ismail, A.F.; Suzaimi, N.D.; Yogarathinam, L.T.; Raji, Y.O.; El-badawy, T.H. Recent development in modification of polysulfone membrane for water treatment application. *J. Water Process Eng.* **2021**, *40*, 101835. [\[CrossRef\]](#)
13. Rana, A.; Sudhaik, A.; Raizada, P.; Khan, A.A.P.; Van Le, Q.; Singh, A.; Selvasembian, R.; Nadda, A.; Singh, P. An overview on cellulose-supported semiconductor photocatalysts for water purification. *Nanotechnol. Environ. Eng.* **2021**, *6*, 40. [\[CrossRef\]](#)
14. Wang, C.; Cheng, P.; Yao, Y.; Yamauchi, Y.; Yan, X.; Li, J.; Na, J. In-situ fabrication of nanoarchitected MOF filter for water purification. *J. Hazard. Mater.* **2020**, *392*, 122164. [\[CrossRef\]](#) [\[PubMed\]](#)
15. Ji, D.; Gao, Y.; Wang, W.; Feng, H.; Chen, K.; Xiao, C. Green preparation of PVDF hollow fiber membranes with multiple pore structure via melt spinning method for oil/water separation. *J. Environ. Chem. Eng.* **2022**, *10*, 108337. [\[CrossRef\]](#)
16. Wang, A.; Li, X.; Hou, T.; Lu, Y.; Zhou, J.; Zhang, X.; Yang, B. A tree-grapes-like PTFE fibrous membrane with superhydrophobic and durable performance for oil/water separation. *Sep. Purif. Technol.* **2021**, *275*, 119165. [\[CrossRef\]](#)
17. Ma, W.; Li, Y.; Gao, S.; Cui, J.; Qu, Q.; Wang, Y.; Huang, C.; Fu, G. Self-healing and superwetable nanofibrous membranes with excellent stability toward multifunctional applications in water purification. *ACS Appl. Mater. Interfaces* **2020**, *12*, 23644–23654. [\[CrossRef\]](#)
18. Nthunya, L.N.; Gutierrez, L.; Derese, S.; Nxumalo, E.N.; Verliefe, A.R.; Mamba, B.B.; Mhlanga, S.D. A review of nanoparticle-enhanced membrane distillation membranes: Membrane synthesis and applications in water treatment. *J. Chem. Technol. Biotechnol.* **2019**, *94*, 2757–2771. [\[CrossRef\]](#)
19. Sagitha, P.; Reshmi, C.R.; Manaf, O.; Sundaran, S.P.; Juraij, K.; Sujith, A. Development of nanocomposite membranes by electrospun nanofibrous materials. In *Nanocomposite Membranes for Water and Gas Separation*; Elsevier: Amsterdam, The Netherlands, 2020; pp. 199–218. [\[CrossRef\]](#)
20. Uddin, Z.; Ahmad, F.; Ullan, T.; Nawab, Y.; Ahmad, S.; Azam, F.; Rasheed, A.; Zafar, M.S. Recent trends in water purification using electrospun nanofibrous membranes. *Int. J. Environ. Sci. Technol.* **2022**, *19*, 9149–9176. [\[CrossRef\]](#)
21. Shahrokhi-Shahraki, R.; Benally, C.; El-Din, M.G.; Park, J. High efficiency removal of heavy metals using tire-derived activated carbon vs commercial activated carbon: Insights into the adsorption mechanisms. *Chemosphere* **2021**, *264*, 128455. [\[CrossRef\]](#)
22. Yuan, Y.; An, Z.; Zhang, R.; Wei, X.; Lai, B. Efficiencies and mechanisms of heavy metals adsorption on waste leather-derived high-nitrogen activated carbon. *J. Clean. Prod.* **2021**, *293*, 126215. [\[CrossRef\]](#)
23. Thambiliyagodage, C. Efficient Photocatalysis of Carbon Coupled TiO₂ to Degrade Pollutants in Wastewater—A Review. *Environ. Nanotechnol. Monit. Manag.* **2022**, *18*, 100737. [\[CrossRef\]](#)
24. Yamakata, A.; Vequizo, J.J.M. Curious Behaviors of Photogenerated Electrons and Holes at the Defects on Anatase, Rutile, and Brookite TiO₂ Powders: A Review. *J. Photochem. Photobiol. C Photochem. Rev.* **2019**, *40*, 234–243. [\[CrossRef\]](#)
25. Qi, W.; Yang, Y.; Du, J.; Yang, J.; Guo, L.; Zhao, L. Highly Photocatalytic Electrospun Zr/Ag Co-Doped Titanium Dioxide Nanofibers for Degradation of Dye. *J. Colloid Interface Sci.* **2021**, *603*, 594–603. [\[CrossRef\]](#)
26. Park, M.; Ko, Y.T.; Ji, M.; Cho, J.S.; Wang, D.H.; Lee, Y.-I. Facile Self-Assembly-Based Fabrication of a Polyvinylidene Fluoride Nanofiber Membrane with Immobilized Titanium Dioxide Nanoparticles for Dye Wastewater Treatment. *J. Clean. Prod.* **2022**, *378*, 134506. [\[CrossRef\]](#)
27. Chen, Y.; Li, A.; Fu, X.; Peng, Z. Electrospinning-Based (N,F)-Co-Doped TiO₂- δ Nanofibers: An Excellent Photocatalyst for Degrading Organic Dyes and Heavy Metal Ions under Visible Light. *Mater. Chem. Phys.* **2022**, *291*, 126672. [\[CrossRef\]](#)
28. Cen, L.; Tang, T.; Yu, F.; Wu, H.; Li, C.; Zhu, H.; Guo, Y. Fabrication of ZIF-8/TiO₂ Electrospinning Nanofibers for Synergistic Photodegradation in Dyeing Wastewater. *J. Ind. Eng. Chem.* **2023**, *126*, 537–545. [\[CrossRef\]](#)
29. Wang, W.; Zhang, G.; Wang, Q.; Meng, F.; Jia, H.; Jiang, W.; Ji, Q. Hybrid Nanoarchitectonics of TiO₂/Aramid Nanofiber Membranes with Softness and Durability for Photocatalytic Dye Degradation. *Chin. Chem. Lett.* **2023**, 109193. [\[CrossRef\]](#)

30. Sun, F.; Qi, H.; Xie, Y.; Ma, Q.; He, W.; Xu, D.; Wang, G.; Yu, W.; Wang, T.; Dong, X. Flexible Self-Supporting Bifunctional [TiO₂/C]/[Bi₂WO₆/C] Carbon-Based Janus Nanofiber Heterojunction Photocatalysts for Efficient Hydrogen Evolution and Degradation of Organic Pollutant. *J. Alloys Compd.* **2020**, *830*, 154673. [CrossRef]
31. Singh, E.; Meyyappan, M.; Nalwa, H.S. Flexible Graphene-Based Wearable Gas and Chemical Sensors. *ACS Appl. Mater. Interfaces* **2017**, *9*, 34544–34586. [CrossRef]
32. Wang, L.; Cheng, Y.; Gopalan, S.; Luo, F.; Amreen, K.; Singh, R.K.; Goel, S.; Lin, Z.; Naidu, R. Review and Perspective: Gas Separation and Discrimination Technologies for Current Gas Sensors in Environmental Applications. *ACS Sens.* **2023**, *8*, 1373–1390. [CrossRef]
33. Krishna, K.G.; Parne, S.; Pothukanuri, N.; Kathirvelu, V.; Gandhi, S.; Joshi, D. Nanostructured Metal Oxide Semiconductor-Based Gas Sensors: A Comprehensive Review. *Sens. Actuators Phys.* **2022**, *341*, 113578. [CrossRef]
34. Yoon, Y.; Truong, P.L.; Lee, D.; Ko, S.H. Metal-Oxide Nanomaterials Synthesis and Applications in Flexible and Wearable Sensors. *ACS Nanosci. Au* **2022**, *2*, 64–92. [CrossRef]
35. Yang, J.; Han, W.; Jiang, B.; Wang, X.; Sun, Y.; Wang, W.; Lou, R.; Ci, H.; Zhang, H.; Lu, G. Electrospinning Derived NiO/NiFe₂O₄ Fiber-in-Tube Composite for Fast Triethylamine Detection under Different Humidity. *ACS Sens.* **2022**, *7*, 995–1007. [CrossRef] [PubMed]
36. Li, Q.; Zeng, W.; Li, Y. NiO-Based Gas Sensors for Ethanol Detection: Recent Progress. *J. Sens.* **2022**, *2022*, 1855493. [CrossRef]
37. Rohman, Y.M.; Sukowati, R.; Priyanto, A.; Hapidin, D.A.; Edikresna, D.; Khairurrijal, K. Quartz Crystal Microbalance Coated with Polyacrylonitrile/Nickel Nanofibers for High-Performance Methanol Gas Detection. *ACS Omega* **2023**, *8*, 13342–13351. [CrossRef]
38. Kampara, R.K.; Sonia, T.; Balamurugan, D.; Jeyaprakash, B.G. Formaldehyde Vapour Sensing Property of Electrospun NiO Nanograins. *Front. Mater. Sci.* **2021**, *15*, 416–430. [CrossRef]
39. Shoukat, N.; Anzar, S.; Asad, M.; Al-Sulami, A.I.; Khalid, H.; Choudhary, A.A.; Sherin, L.; Akhtar, N. Fabrication of CuO–NiO Wrapped Cellulose Acetate/Polyaniline Electrospun Nanofibers for Sensitive Monitoring of Bisphenol-A. *ACS Sustain. Chem. Eng.* **2023**, *11*, 4299–4307. [CrossRef]
40. Wu, L.; Song, Y.; Xing, S.; Li, Y.; Xu, H.; Yang, Q.; Li, Y. Advances in Electrospun Nanofibrous Membrane Sensors for Ion Detection. *RSC Adv.* **2022**, *12*, 34866–34891. [CrossRef]
41. Blachowicz, T.; Ehrmann, A. Most Recent Developments in Electrospun Magnetic Nanofibers: A Review. *J. Eng. Fibers Fabr.* **2020**, *15*, 155892501990084. [CrossRef]
42. Gan, Y.; Yu, C.; Panahi, N.; Gan, J.; Cheng, W. Processing Iron Oxide Nanoparticle-Loaded Composite Carbon Fiber and the Photosensitivity Characterization. *Fibers* **2019**, *7*, 25. [CrossRef]
43. Liu, H.-Y.; Xu, L.; Tang, X.-P.; Sun, Z.Q. Effect of Fe₃O₅ Nanoparticles on Magnetic Electrospun Nanofibers. *J. Text. Inst.* **2015**, *106*, 503–509. [CrossRef]
44. Shi, S.; Xu, C.; Wang, X.; Xie, Y.; Wang, Y.; Dong, Q.; Zhu, L.; Zhang, G.; Xu, D. Electrospinning Fabrication of Flexible Fe₃O₄ Fibers by Sol-Gel Method with High Saturation Magnetization for Heavy Metal Adsorption. *Mater. Des.* **2020**, *186*, 108298. [CrossRef]
45. Shi, S.; Xu, C.; Dong, Q.; Wang, Y.; Zhu, S.; Zhang, X.; Tak Chow, Y.; Wang, X.; Zhu, L.; Zhang, G.; et al. High Saturation Magnetization MnO₂/PDA/Fe₃O₄ Fibers for Efficient Pb(II) Adsorption and Rapid Magnetic Separation. *Appl. Surf. Sci.* **2021**, *541*, 148379. [CrossRef]
46. Teng, Y.; Li, Y.; Li, Y.; Song, Q. Preparation of Fe₃O₄/PVP Magnetic Nanofibers via in Situ Method with Electro-spinning. *J. Phys. Conf. Ser.* **2020**, *1549*, 032087. [CrossRef]
47. Liu, J.; Chang, M.-J.; Du, H.-L. Facile Preparation of Cross-Linked Porous Poly(Vinyl Alcohol) Nanofibers by Electrospinning. *Mater. Lett.* **2016**, *183*, 318–321. [CrossRef]
48. Wang, S.; Wang, C.; Zhang, B.; Sun, Z.; Li, Z.; Jiang, X.; Bai, X. Preparation of Fe₃O₄/PVA Nanofibers via Com-bining in-Situ Composite with Electrospinning. *Mater. Lett.* **2010**, *64*, 9–11. [CrossRef]
49. Konwar, A.; Gogoi, A.; Chowdhury, D. Magnetic Alginate–Fe₃O₄ Hydrogel Fiber Capable of Ciprofloxacin Hydrochloride 1161 Adsorption/Separation in Aqueous Solution. *RSC Adv.* **2015**, *5*, 81573–81582. [CrossRef]
50. Mansurov, Z.; Smagulova, G.; Kaidar, B.; Imash, A.; Lesbayev, A. PAN—Composite Electrospun-Fibers Decorated with Magnetite Nanoparticles. *Magnetochemistry* **2022**, *8*, 160. [CrossRef]
51. Prikhod'ko, N.G.; Smagulova, G.T.; Nazhipkyzy, M.; Rakhymzhan, N.B.; Temirgalieva, T.S.; Lesbaev, B.T.; Zakhidov, A.A.; Mansurov, Z.A. High-Efficiency Selective Solar Absorber from Nanostructured Carbonized Plant Raw Material. *J. Eng. Phys. Thermophys.* **2020**, *93*, 1020–1029. [CrossRef]
52. Liang, L.; Huang, W.; Gao, F.; Hao, X.; Zhang, Z.; Zhang, Q.; Guan, G. Mild Catalytic Depolymerization of Low Rank Coals: A Novel Way to Increase Tar Yield. *RSC Adv.* **2015**, *5*, 2493–2503. [CrossRef]
53. Karika, J.C. Characterization of Graphitization in Coal Tar and Petroleum Pitches. Master's Thesis, Arizona State University, Tempe, AZ, USA, 1985. Available online: <https://apps.dtic.mil/sti/citations/ADA166942> (accessed on 2 April 2023).
54. Ali, B.; Tasirin, S.; Aminayi, P.; Yaakob, Z.; Ali, N.; Noori, W. Non-Supported Nickel-Based Coral Sponge-Like Porous Magnetic Alloys for Catalytic Production of Syngas and Carbon Bio-Nanofilaments via a Biogas De-composition Approach. *Nanomaterials* **2018**, *8*, 1053. [CrossRef] [PubMed]

55. Zaitseva, N.V.; Zemlyanova, M.A.; Zvezdin, V.N.; Dovbysh, A.A.; Ulanova, T.S.; Smirnov, S.A.; Stepankov, M.S. Comparative Assessment of the Effects of Short-Term Inhalation Exposure to Nickel Oxide Nanoparticles and Microdispersed Nickel Oxide. *Nanotechnol. Russ.* **2016**, *11*, 671–677. [[CrossRef](#)]
56. Mokoena, T.P.; Swart, H.C.; Motaung, D.E. A Review on Recent Progress of P-Type Nickel Oxide Based Gas Sensors: Future Perspectives. *J. Alloys Compd.* **2019**, *805*, 267–294. [[CrossRef](#)]
57. Gao, Y.; Zhang, J.; Leng, D.; Li, G.; Zhang, Y.; Wang, W.; Liang, Q.; Chen, X.; Lu, H.; Gao, J. Electrospun NiO Nanofibers with Rh Decoration for Enhanced Acetone Sensing Performances. *J. Mater. Sci. Mater. Electron.* **2021**, *32*, 14102–14112. [[CrossRef](#)]
58. Fan, X.; Xu, Y.; He, W. High Acetone Sensing Properties of In₂O₃–NiO One-Dimensional Heterogeneous Nanofibers Based on Electrospinning. *RSC Adv.* **2021**, *11*, 11215–11223. [[CrossRef](#)]
59. Zhang, R.; Shi, J.; Zhou, T.; Tu, J.; Zhang, T. A Yolk-Double-Shelled Heterostructure-Based Sensor for Acetone Detecting Application. *J. Colloid Interface Sci.* **2019**, *539*, 490–496. [[CrossRef](#)]
60. Yang, J.; Han, W.; Ma, J.; Wang, C.; Shimano, K.; Zhang, S.; Sun, Y.; Cheng, P.; Wang, Y.; Zhang, H.; et al. Sn Doping Effect on NiO Hollow Nanofibers Based Gas Sensors about the Humidity Dependence for Triethylamine Detection. *Sens. Actuators B Chem.* **2021**, *340*, 129971. [[CrossRef](#)]
61. Soleimanpour, A.M.; Jayatissa, A.H.; Sumanasekera, G. Surface and Gas Sensing Properties of Nanocrystalline Nickel Oxide Thin Films. *Appl. Surf. Sci.* **2013**, *276*, 291–297. [[CrossRef](#)]
62. Marikutsa, A.; Rummyantseva, M.; Konstantinova, E.A.; Gaskov, A. The Key Role of Active Sites in the Development of Selective Metal Oxide Sensor Materials. *Sensors* **2021**, *21*, 2554. [[CrossRef](#)]
63. Nikolic, M.V.; Milovanovic, V.; Vasiljevic, Z.Z.; Stamenkovic, Z. Semiconductor Gas Sensors: Materials, Technology, Design, and Application. *Sensors* **2020**, *20*, 6694. [[CrossRef](#)]
64. Mahadadalkar, M.A.; Park, N.; Yusuf, M.; Nagappan, S.; Nallal, M.; Park, K.H. Electrospun Fe Doped TiO₂ Fiber Photocatalyst for Efficient Wastewater Treatment. *Chemosphere* **2023**, *330*, 138599. [[CrossRef](#)] [[PubMed](#)]
65. Cheng, H.; Zhang, W.; Liu, X.; Tang, T.; Xiong, J. Fabrication of Titanium Dioxide/Carbon Fiber (TiO₂/CF) Composites for Removal of Methylene Blue (MB) from Aqueous Solution with Enhanced Photocatalytic Activity. *J. Chem.* **2021**, *2021*, 9986158. [[CrossRef](#)]
66. Cao, N.; Gu, M.; Gao, M.; Li, C.; Liu, K.; Zhao, X.; Feng, J.; Ren, Y.; Wei, T. A Three-Layer Photocatalyst Carbon Fibers/TiO₂ Seed/TiO₂ Nanorods with High Photocatalytic Degradation under Visible Light. *Appl. Surf. Sci.* **2020**, *530*, 147289. [[CrossRef](#)]
67. Basit, M.A.; Raza, F.; Ali, G.; Parveen, A.; Khan, M.; Park, T.J. Nanoscale Modification of Carbon Fibers with CdS Quantum-Dot Sensitized TiO₂: Photocatalytic and Photothermal Evaluation under Visible Irradiation. *Mater. Sci. Semicond. Process.* **2022**, *142*, 106485. [[CrossRef](#)]
68. Santos, J.D.; Sato, T.P.; Lima, A.L.D.; Nogueira, A.S.; Quishida, C.C.C.; Borges, A.L.S. Titanium Dioxide and Polyethylmethacrylate Electrospun Nanofibers: Assessing the Technique Parameters and Morphological Characterization. *Braz. Dent. Sci.* **2019**, *22*, 70–78. [[CrossRef](#)]
69. Wang, X.; Xu, L.; Zheng, G.; Jiang, J.; Sun, D.; Li, W. Formation of Suspending Beads-on-a-String Structure in Electrohydrodynamic Printing Process. *Mater. Des.* **2021**, *204*, 109692. [[CrossRef](#)]
70. Covaliu-Mierla, C.I.; Matei, E.; Stoian, O.; Covaliu, L.; Constandache, A.-C.; Iovu, H.; Paraschiv, G. TiO₂—Based Nanofibrous Membranes for Environmental Protection. *Membranes* **2022**, *12*, 236. [[CrossRef](#)]
71. Maruccia, E.; Ferrari, S.; Bartoli, M.; Lucherini, L.; Meligrana, G.; Pirri, C.F.; Saracco, G.; Gerbaldi, C. Effect of Thermal Stabilization on PAN-Derived Electrospun Carbon Nanofibers for CO₂ Capture. *Polymers* **2021**, *13*, 4197. [[CrossRef](#)]
72. Hassan, M.F.; Sabri, M.A.; Fazal, H.; Hafeez, A.; Shezad, N.; Hussain, M. Recent trends in activated carbon fibers production from various precursors and applications—A comparative review. *J. Anal. Appl. Pyrolysis* **2020**, *145*, 104715. [[CrossRef](#)]
73. Yuan, Y.; Chen, Z.; Yu, H.; Zhang, X.; Liu, T.; Xia, M.; Zheng, R.; Shui, M.; Shu, J. Heteroatom-doped carbon-based materials for lithium and sodium ion batteries. *Energy Storage Mater.* **2020**, *32*, 65–90. [[CrossRef](#)]
74. Martins, I.M.; Sampaio, A.G.; Lima, G.M.; Oliveira e Campos, M.A.; Rodgher, S.; Rodrigues-Siqueli, A.C.; Baldan, M.R.; Marcuzzo, J.S.; Koga-Ito, C.Y. Application of textile (PAN-based) activated carbon fibers decorated with silver nanoparticles in water treatment. *Front. Environ. Sci.* **2023**, *10*, 1100583. [[CrossRef](#)]
75. Yang, K.; Pan, T.; Zhao, Q.; Chen, C.; Zhu, X.; Wang, P.; Chen, B. Dual-function ultrafiltration membrane constructed from pure activated carbon particles via facile nanostructure reconstruction for high-efficient water purification. *Carbon* **2020**, *168*, 254–263. [[CrossRef](#)]
76. Abdullah, N.; Othman, F.E.C.; Yusof, N.; Matsuura, T.; Lau, W.J.; Jaafar, J.; Ismail, A.F.; Salleh, W.N.W.; Aziz, F. Preparation of nanocomposite activated carbon nanofiber/manganese oxide and its adsorptive performance toward leads (II) from aqueous solution. *J. Water Process Eng.* **2020**, *37*, 101430. [[CrossRef](#)]
77. Ji, Y.; Wang, X. Purification performance of modified polyacrylonitrile fiber-activated carbon fiber filter for heavy metal ions. *Environ. Sci. Pollut. Res.* **2023**, *30*, 23372–23385. [[CrossRef](#)]
78. Yunus, Z.M.; Al-Gheethi, A.; Othman, N.; Hamdan, R.; Ruslan, N.N. Removal of heavy metals from mining effluents in tile and electroplating industries using honeydew peel activated carbon: A microstructure and techno-economic analysis. *J. Clean. Prod.* **2020**, *251*, 119738. [[CrossRef](#)]
79. Nordin, N.A.; Abdul Rahman, N.; Abdullah, A.H. Effective removal of Pb(II) ions by electrospun PAN/Sago lignin-based activated carbon nanofibers. *Molecules* **2020**, *25*, 3081. [[CrossRef](#)]

80. Deng, Z.; Sun, S.; Li, H.; Pan, D.; Patil, R.R.; Guo, Z.; Seok, I. Modification of coconut shell-based activated carbon and purification of wastewater. *Adv. Compos. Hybrid Mater.* **2021**, *4*, 65–73. [[CrossRef](#)]
81. Sakamoto, T.; Amano, Y.; Machida, M. Phosphate Ion Adsorption Properties of PAN-Based Activated Carbon Fiber Prepared with Na₂CO₃ Activation. *J. Water Chem. Technol.* **2021**, *43*, 298–304. [[CrossRef](#)]
82. Zuo, Q.; Zheng, H.; Zhang, P.; Zhang, Y. Functionalized activated carbon fibers by hydrogen peroxide and polydopamine for efficient trace lead removal from drinking water. *Langmuir* **2021**, *38*, 253–263. [[CrossRef](#)]
83. Kim, D.W.; Wee, J.H.; Yang, C.M.; Yang, K.S. Efficient removals of Hg and Cd in aqueous solution through NaOH-modified activated carbon fiber. *Chem. Eng. J.* **2020**, *392*, 123768. [[CrossRef](#)]
84. Chen, B.C.; Tsai, C.Y.; Pan, S.Y.; Chen, Y.T.; Hsi, H.C. Sustainable recovery of gaseous mercury by adsorption and electrothermal desorption using activated carbon fiber cloth. *Environ. Sci. Technol.* **2020**, *54*, 1857–1866. [[CrossRef](#)] [[PubMed](#)]
85. Adekola, F.A.; Hodonou, D.S.S.; Adegoke, H.I. Thermodynamic and Kinetic Studies of Biosorption of Iron and Manganese from Aqueous Medium Using Rice Husk Ash. *Appl. Water Sci.* **2016**, *6*, 319–330. [[CrossRef](#)]
86. Abdeen, Z.; Mohammad, S.G.; Mahmoud, M.S. Adsorption of Mn (II) Ion on Polyvinyl Alcohol/Chitosan Dry Blending from Aqueous Solution. *Environ. Nanotechnol. Monit. Manag.* **2015**, *3*, 1–9. [[CrossRef](#)]
87. Tavlieva, M.P.; Genieva, S.D.; Georgieva, V.G.; Vlaev, L.T. Thermodynamics and Kinetics of the Removal of Manganese(II) Ions from Aqueous Solutions by White Rice Husk Ash. *J. Mol. Liq.* **2015**, *211*, 938–947. [[CrossRef](#)]
88. Ali, A.; Saeed, K. Decontamination of Cr(VI) and Mn(II) from Aqueous Media by Untreated and Chemically Treated Banana Peel: A Comparative Study. *Desalin. Water Treat.* **2015**, *53*, 3586–3591. [[CrossRef](#)]

Disclaimer/Publisher's Note: The statements, opinions and data contained in all publications are solely those of the individual author(s) and contributor(s) and not of MDPI and/or the editor(s). MDPI and/or the editor(s) disclaim responsibility for any injury to people or property resulting from any ideas, methods, instructions or products referred to in the content.